HHS Public Access

Author manuscript

Nature. Author manuscript; available in PMC 2020 January 01.

Published in final edited form as:

Nature. 2019 July ; 571(7764): 284–288. doi:10.1038/s41586-019-1355-4.

Smoothened stimulation by membrane sterols drives Hedgehog pathway activity

Ishan Deshpande[1], **Jiahao Liang**[1], **Danielle Hedeen**[2,3], **Kelsey J. Roberts**[4,5], **Yunxiao Zhang**[4], **Betty Ha**[6,7,8,9], **Naomi R. Latorraca**[6,7,8,9,10], **Bryan Faust**[1], **Ron O. Dror**[6,7,8,9,10], **Philip A. Beachy**[4,5,11,12], **Benjamin R. Myers**[4,14,15,*], **Aashish Manglik**[1,13,*]

[1]Department of Pharmaceutical Chemistry, University of California, San Francisco, San Francisco, CA, USA.

[2]Department of Oncological Sciences, University of Utah School of Medicine, Salt Lake City, UT, USA.

[3]Huntsman Cancer Institute, University of Utah School of Medicine, Salt Lake City, UT, USA.

[4]Institute for Stem Cell Biology and Regenerative Medicine, Stanford University School of Medicine, Stanford, CA, USA.

[5]Department of Developmental Biology, Stanford University School of Medicine, Stanford, CA, USA.

[6]Department of Molecular and Cellular Physiology, Stanford University School of Medicine, Stanford, CA, USA.

[7]Department of Structural Biology, Stanford University School of Medicine, Stanford, CA, USA.

[8]Department of Computer Science, Stanford University, Stanford, CA, USA.

[*]**Correspondence and requests for materials** should be addressed to B.R.M. or A.M. Benjamin.Myers@hci.utah.edu; Aashish.Manglik@ucsf.edu.

Author contributions I.D. developed purification approaches for wild-type mSMO, characterized the effect of NbSmo8 on SAG21k affinity, performed crystallization trials, collected diffraction data, determined and refined the structure, and performed fluorescence size-exclusion experiments. J.L. assisted with yeast surface display selections, expressed and purified NbSmo8, and performed fluorescence size-exclusion experiments. D.H. performed NbSmo8 imaging experiments. K.J.R. and Y.Z. performed signalling studies for SMO mutants under guidance from PA.B. Y.Z. also assisted with yeast surface display selections. B.H. and N.R.L. performed and analysed molecular dynamics simulations under the guidance of R.O.D. B.R.M. performed preliminary experiments establishing SMO nanobodies as intracellular biosensors as a postdoctoral fellow with input and support from P.A.B. B.F. and I.D. performed surface plasmon resonance experiments. I.D., B.R.M. and A.M. wrote the manuscript with revisions provided by P.A.B. A.M. purified SMO and performed yeast selection, identified individual nanobodies, refined the structure and supervised the overall project.

Online content

Any methods, additional references, Nature Research reporting summaries, source data, extended data, supplementary information, acknowledgements, peer review information; details of author contributions and competing interests; and statements of data and code availability are available at https://doi.org/10.1038/s41586–019-1355–4.

Data availability

All data generated or analysed during this study are included in the published Letter and its Supplementary Information. Crystallographic coordinates and structure factors for the SMO-SAG21k-NbSmo8 complex have been deposited in the PDB under accession code 6O3C.

Competing interests The authors declare no competing interests.

Additional information

Supplementary information is available for this paper at https://doi.org/10.1038/s41586–019-1355–4.

Peer review information *Nature* thanks Raymond Stevens and the other anonymous reviewer(s) for their contribution to the peer review of this work.

[9]Institute for Computational and Mathematical Engineering, Stanford University, Stanford, CA, USA.

[10]Biophysics Program, Stanford University, Stanford, CA, USA.

[11]Department of Urology, Stanford University School of Medicine, Stanford, CA, USA.

[12]Chemical and Systems Biology, Stanford University School of Medicine, Stanford, CA, USA.

[13]Department of Anesthesia and Perioperative Care, University of California, San Francisco, San Francisco, CA, USA.

[14]Department of Oncological Sciences, University of Utah School of Medicine, Salt Lake City, UT, USA.

[15]Huntsman Cancer Institute, University of Utah School of Medicine, Salt Lake City, UT, USA.

Abstract

Hedgehog signalling is fundamental to embryonic development and postnatal tissue regeneration[1]. Aberrant postnatal Hedgehog signalling leads to several malignancies, including basal cell carcinoma and paediatric medulloblastoma[2]. Hedgehog proteins bind to and inhibit the transmembrane cholesterol transporter Patched-1 (PTCH1), which permits activation of the seven-transmembrane transducer Smoothened (SMO) via a mechanism that is poorly understood. Here we report the crystal structure of active mouse SMO bound to both the agonist SAG21k and to an intracellular binding nanobody that stabilizes a physiologically relevant active state. Analogous to other G protein-coupled receptors, the activation of SMO is associated with subtle motions in the extracellular domain, and larger intracellular changes. In contrast to recent models[3–5], a cholesterol molecule that is critical for SMO activation is bound deep within the seven-transmembrane pocket. We propose that the inactivation of PTCH1 by Hedgehog allows a transmembrane sterol to access this seven-transmembrane site (potentially through a hydrophobic tunnel), which drives the activation of SMO. These results—combined with signalling studies and molecular dynamics simulations—delineate the structural basis for PTCH1 -SMO regulation, and suggest a strategy for overcoming clinical resistance to SMO inhibitors.

The Hedgehog (Hh) signal is transduced across the plasma membrane by an unusual mechanism. In the pathway ‘off’ state, PTCH1 suppresses SMO, an oncoprotein and a member of the class F G protein-coupled-receptor (GPCR) superfamily. Hh proteins initiate intracellular signalling by binding to and inhibiting PTCH1, which thereby unleashes SMO. Upon activation, SMO accumulates in the vertebrate primary cilium, and ultimately activates glioma-associated (GLI) transcription factors. The unusually deep seven-transmembrane (7TM) pocket of SMO is the target of naturally occurring and synthetic small molecules that include the antagonists cyclopamine, vismodegib and SANT-1, as well as agonists (such as SAG21k) that activate SMO even in the presence of PTCH1.

Despite the central role of SMO in Hh signal transduction, the precise mechanism underlying SMO activation remains poorly defined. A longstanding model suggests that PTCH1 regulates SMO by controlling its access to a lipid modulator within the plasma membrane[6]. More recent work supports this view, providing increasing evidence that

cholesterol or a related sterol is critical for SMO activation. Cholesterol is sufficient for SMO activation both in cells and in vitro with purified components[3,7–11]. Structural and cell biological studies have shown that PTCH1 is a transmembrane transporter with multiple sterol-binding sites and that it can directly reduce cholesterol levels in the inner leaflet of the plasma membrane[12]; Hh binding to PTCH1 blocks this activity[12–14]. However, how PTCH1-mediated changes in the level of cholesterol in the inner leaflet lead to SMO activation remains unknown. Furthermore, although cholesterol is sufficient to fully activate SMO, the identity of the physiological SMO effector remains unclear. Recent structural studies of SMO have identified a sterol that is bound within the extracellular cysteine-rich domain (CRD)[4,7]. Biochemical and functional studies in a range of experimental systems suggest that this CRD sterol site is important for SMO activation, and have led to the proposal that PTCH1 operates directly on this site to control SMO activity[3–5]. However, this model does not account for results demonstrating SMO mutants that contain CRD point mutations or deletions retain sensitivity to both PTCH1 action and alterations in membrane cholesterol[7,10,11,15]. We therefore speculated that PTCH1 regulates SMO by operating primarily on a sterol-binding site within the 7TM domain that is, as yet, undefined. To better understand SMO activation, we determined the structure of SAG21k-bound SMO stabilized in an active state by a conformation-specific, single-domain antibody (nanobody).

Because agonist-bound GPCRs are highly dynamic, capturing fully active, signalling-competent conformations in structural studies has generally required the use of downstream signalling transducers or antibody fragments that stabilize the active state[16]. Although the physiological role of G protein coupling in SMO signalling remains controversial[17], we reasoned that active SMO may share the dynamic properties of the broader GPCR family[10]. We therefore developed nanobodies that preferentially bind active SMO using a yeast surface-displayed synthetic nanobody library[18] (Fig. 1a). NbSmo8, one of the clones from this library, bound agonist (SAG21k)-occupied SMO but not apo or antagonist-occupied SMO, as assessed by both yeast display and size-exclusion chromatography (Fig. 1b, Extended Data Fig. 1a, b). In surface plasmon resonance experiments, immobilized NbSmo8 bound SAG21k-occupied SMO (dissociation constant, K_D = 117 nM) but showed no detectable interaction with antagonist (SANT-1)-occupied SMO (Fig. 1c). SMO purified within cholesterol-laden detergent micelles also bound NbSmo8 (K_D = 168 nM) (Fig. 1c, Extended Data Fig. 1c), consistent with cholesterol-driven activation of SMO in cells. We next tested whether NbSmo8 recognizes active SMO in a native membrane environment by co-expressing SMO with NbSmo8-GFP in HEK293 cells that lack exogenous PTCH1; under these conditions, SMO is constitutively active[10]. Here, NbSmo8 resides at the membrane (Fig. 1d, e, Extended Data Fig. 1d) but relocalizes to the cytoplasm upon SMO inactivation via pharmacological depletion of cholesterol, treatment with KAAD-cyclopamine or coexpression with PTCH1. Thus, NbSmo8 plasma membrane recruitment faithfully reflects the activation state of SMO that is observed in conventional downstream GLI-based assays. Co-immunoprecipitation of NbSmo8 with active—but not inactive—SMO further confirmed these imaging results (Extended Data Fig. 1e). NbSmo8 therefore selectively binds a physiologically relevant active SMO conformation both in vitro and in cells.

For structural studies, we established approaches to purify minimally modified mouse SMO (mSMO) without fusion protein insertions, deglycosylation mutations or thermostabilizing

mutations. Wild-type mSMO with truncations in N-and C-terminal residues that are dispensable for SMO conformational activation in vitro and PTCH1 inhibition in vivo[10] was purified in complex with SAG21k and NbSmo8. Crystals were obtained in a lipidic mesophase derived from 10/1 ratio of monoolein/cholesterol. Merging diffraction data from 20 crystals yielded a structure at a resolution of 2.8 Å (Extended Data Table 1).

NbSmo8 binds the SMO 7TM domain intracellularly (Fig. 2a, Extended Data Fig. 2), stabilizing conformational changes that are generally associated with GPCR activation[19]. Compared to previously published structures of inactive human SMO (hSMO)[7,20,21], active mSMO displays an outward displacement of transmembrane helix 6 (TM6) of 8 Å and an inward movement of TM5 of 6 Å (Fig. 2b, c, Extended Data Fig. 3). These changes are similar—but not identical—to recently published structures of *Xenopus* SMO (xSMO) bound to cholesterol or the atypical SMO antagonist cyclopamine[4,22] in the absence of intracellular binding partners that are generally required to capture 7TM proteins in their active conformations. Key differences between these xSMO structures and the structure presented here include lateral displacements of TM5 and TM6. Although it is challenging to ascribe a specific consequence of these differences to changes in SMO activation, we speculate that the 7TM domain in the xSMO structures is in an active-like intermediate state. This may explain the ability of cyclopamine to induce ciliary accumulation without signalling to G proteins and to GLI[10,22–24]. The ability of NbSmo8 to selectively recognize active SMO in vitro and in vivo provides confidence in the physiological relevance of the NbSmo8-stabilized SMO state.

We identified a sterol that is bound deep within the 7TM core of active SMO (Fig. 3a, b). Although the electron density precludes unambiguous assignment of this sterol, it is most likely to be cholesterol from the lipidic cubic phase used for crystallization, which contained 10 mol% cholesterol. Although cholesteryl hemisuccinate was used to purify SMO, the extended hemisuccinate tail is not observed in the electron density at the 7TM site. Cellular sterols could remain bound to SMO during purification; however, our initial purification steps involving vismodegib would displace sterol binding at this site (see below). Previous structures probably failed to resolve a 7TM sterol because they captured inactive or intermediate SMO conformations or introduced mutations (for example, hSMO(V329F)) that would directly preclude sterol binding. Although the sterol in our structure is probably cholesterol, it remains possible that other sterols—including cilia-associated oxysterols[25]—may bind and activate SMO through this deep 7TM site.

Recent studies[3–5] have emphasized sterol binding to the SMO CRD as the critical event that is controlled by PTCH1 in Hh signalling. This model invokes two energetically unfavourable and unlikely events: cholesterol must traverse charged regions in the upper SMO 7TM pocket, and desolvate from the membrane bilayer to bind to the CRD. Here we propose that the deep 7TM site is the primary mediator of sterol action in SMO signalling for several reasons. First, 7TM-bound cholesterol favours SMO activation by stabilizing an outward displacement of TM6, whereas inactive SMO would preclude binding of cholesterol at this site. Such direct TM6 stabilization is similar to the activation mechanism of other GPCRs by agonists[19]. By contrast, the relatively minor modulatory effect exerted by cholesterol at other GPCRs probably results from cholesterol binding to shallower sites outside of the 7TM

bundle (Extended Data Fig. 4). Second, molecular dynamics simulations of active SMO bound to 7TM cholesterol (but in the absence of SAG21k and NbSmo8) revealed that the modelled cholesterol bound stably within the 7TM site over multiple independent simulations, each approximately 0.8 μs in length (Fig. 3c, Extended Data Fig. 5a). Even without NbSmo8 or SAG21k, cholesterol-bound SMO remained in the active conformation with an outward displacement of TM6 throughout each of these same simulations (Extended Data Fig. 5b), which suggests that cholesterol within the 7TM site may be sufficient to stabilize active SMO. Finally, mutation of residues deep within the 7TM site[21] to bulkier side chains predicted to preclude sterol binding (including mSMO V333F, V408F, I412F and T470Q) ablated GLI activation, both by SAG21k and by native Sonic hedgehog (ShhNp) (Fig. 3d). Specific ablation of a hydrogen bond between cholesterol and SMO in the mSMO(Y398F) mutant also decreased the ability of SMO to activate GLI (Fig. 3e). We next tested whether sterols directly activate SMO via the 7TM site, both in cells and using purified components. Cholesterol delivered in complex with methyl-β-cyclodextrin activates GLI to levels that are similar to those activated with 0.6 nM ShhNp (Fig. 3f). Mutations that target the 7TM site (mSMO V333F and T470Q) result in a complete loss of cholesterol-induced GLI activation, even in the context of PTCH1 inhibition by ShhNp. In size-exclusion chromatography experiments, NbSmo8 robustly bound to wild-type SMO purified in cholesterol-laden detergent micelles (Fig. 3g). Cholesterol-enabled binding of NbSmo8 was fully reversed by the V333F mutation, which demonstrates the importance of sterol binding at the 7TM site in the conformational activation of SMO. All of the tested mutants robustly bound BODIPY-cyclopamine[22], which indicates that they fold and traffic to the cellular membrane normally (Extended Data Fig. 6). The deep 7TM site is therefore directly required for sterol-mediated activation of SMO.

Membrane sterols may access the 7TM site via a hydrophobic tunnel between TM5 and TM6 of active SMO that opens to the inner leaflet of the membrane bilayer (Fig. 3h). The location of this conduit in active mSMO is almost identical to a tunnel that has recently been observed[4] (RCSB Protein Data Bank (PDB) code 6D32) for xSMO (Extended Data Fig. 7), and may enable sterols to activate SMO without the energetically prohibitive step of membrane desolvation. The position of the cholesterol hydroxyl in active SMO suggests that access to this tunnel from the inner leaflet would require a flip in sterol orientation en route to the 7TM site. We designed two mutations to occlude the entrance to this tunnel: mSMO(A463F), which rendered SMO unresponsive to stimulation by ShhNp, and mSMO(G420F), which only partially reduced the response to ShhNp (Fig. 3d). The difference between these mutants may relate to differences in the extent of tunnel occlusion. The access of agonists to the interior of the 7TM bundle directly from the membrane has precedent in other lipid-activated GPCRs[26]. The structurally observed hydrophobic tunnel may therefore be an important conduit for sterol entry into the 7TM bundle, which provides a potential mechanism for the specific action of inner-leaflet sterols on the 7TM sterol-binding site that we identify here.

The 7TM cholesterol occupies the deepest portion of the SMO 7TM pocket (Fig. 3a, b). Most co-crystallized SMO antagonists bind towards the extracellular side of the inactive SMO 7TM pocket but extend a functional group into the deeper sterol site (Fig. 4a), and thereby probably preclude sterol binding. In contrast to the other antagonists, SANT-1

extensively overlaps with cholesterol (Fig. 4b). Unlike an activating sterol, SANT-1 contacts H470 of hSMO (H474 of mSMO) in TM6, which stabilizes the inward, inactive conformation[21] (Extended Data Fig. 8a). Previously published[27] structure-activity relationships of the SAG agonist further underscore the importance of 7TM sterol competition in SMO antagonism (Extended Data Fig. 8b). The substitution of the 4-aminomethyl group of SAG with larger aliphatic groups converts SAG into a SMO antagonist[27]. All of these groups are predicted to extend deeper into the 7TM pocket and directly compete with a bound sterol, which demonstrates that even an otherwise-activating chemical scaffold inactivates SMO if the 7TM cholesterol is displaced.

In Hh-driven cancers, prolonged treatment with SMO inhibitors frequently selects for resistance mutations, which renders SMO insensitive to clinically used antagonists[2]. A number of resistance mutations line the 7TM pocket and directly influence inhibitor binding. Other mutations occur at potential allosteric sites, some of which we now map to the 7TM sterol pocket (Extended Data Fig. 9). As has previously been reported, the majority of SMO resistance mutants are sensitive to PTCH1 action[11], which suggests that these SMO mutants continue to require PTCH1-regulated sterols for activation. The majority of Hh-driven tumours arise from loss-of-function mutations in PTCH1, which leaves intact the necessity for sterols in SMO activation and consequent stimulation of tumour growth. On the basis of the direct role of 7TM sterol binding in SMO activation, we propose that SMO antagonists such as SANT-1—which are isosteric with the co-crystallized 7TM cholesterol (Fig. 4b)—would be less susceptible to resistance mutations that block antagonist binding, as these mutations would be likely to also prevent sterol binding and activation of SMO.

SAG and its derivatives activate SMO in cell-based and reconstituted systems, and this activity is potentiated by cholesterol[10,11,15,28]. Indeed, SAG21k synergizes with cholesterol to increase the binding of NbSmo8 to SMO (Extended Data Fig. 1c). These effects bear the hallmarks of a GPCR positive allosteric modulator, and are rationalized by the non-overlapping—but closely apposed—binding sites for SAG21k and the 7TM cholesterol (Fig. 3a). SAG21k occupies a site that is similar to that previously observed for inactive hSMO bound to SAG1.5[21], with the 4-amino group making an ionic interaction with mSMO D477 and E522 (Fig. 4c). In contrast to SAG1.5, SAG21k in active SMO is displaced towards the extracellular side, and thereby stabilizes an upward helical displacement of extracellular loop (ECL) 3 and TM6 in active SMO (Fig. 4d).

As in previously determined structures[3,4,7,29], activated SMO binds a sterol within the conserved CRD lipid-binding site of class F GPCRs (Fig. 4e, f). Sterol binding to the CRD has previously been shown to activate SMO—most notably, binding by oxysterols such as 20(*S*)-hydroxycholesterol and 7β−27-hydroxycholesterol[11,25,29,30]. A resolved *N*-acetyl glucosamine on mSMO N497 forms part of the CRD sterol pocket and probably relays sterol binding within the CRD to the rest of ECL3. Unique to SMO among the GPCR family, the entire ECL3-TM6 helix is displaced by 3 Å towards the extracellular side compared to inactive SMO (Figs. 2b, 4e). The observed upward shift in ECL3 towards the CRD is relayed directly to TM6, which illustrates how the CRD can regulate SMO activation. This coupling of ECL3 to TM6 in SMO is probably responsible for the complex

allosteric communication between three distinct ligand-binding sites (the deep 7TM sterol pocket, the SAG21k or cyclopamine site and the CRD sterol pocket).

Recent xSMO structures[4] displayed a 120° rotation of the CRD, which is potentially associated with SMO activation. Comparison of all inactive-state hSMO structures revealed a maximal rotational range of motion of about 20° along a common axis; the CRD of active mSMO presented here is positioned intermediately between the largest degree of rotational motion in vismodegib-bound hSMO and apo hSMO. By contrast, the xSMO CRD rotates along an axis that is different from the rotational axis in other SMO structures (Fig. 4g). One possible explanation is that the mutation of the ECL3 glycosylation site in xSMO leads to a loss of critical interactions that are necessary for stabilizing the CRD as it is positioned in all other SMO structures. Importantly, the structure of active mSMO suggests that the considerable reorientation of the CRD in xSMO is not specifically required for the activation of mammalian SMO.

Mutational analysis supports an important role for the SMO CRD in Hh pathway activity. Point mutations in the CRD sterol-binding site (mSMO D99A and Y134F), or complete deletion of the CRD, have previously been shown to abolish activation by oxysterols or by exogenous cholesterol delivered as a cyclodextrin inclusion complex[7,9,10]. However, these mutants can be activated by SMO agonists or by Hh—albeit to a reduced extent[7,10]. This stands in contrast to mutations that disrupt the 7TM sterol site, which eliminate cholesterol-, Hh-and SAG21k-mediated activation of SMO. We therefore speculate that the activation of SMO by a 7TM-binding sterol leads to an outward and upward displacement of TM6, which is further stabilized by sterol binding to the CRD.

The structure of activated SMO enabled identification of a sterol-binding site deep within the 7TM domain. SMO antagonists directly block binding of sterols at this site. Synthetic agonists such as SAG21k favour an active SMO conformation, and at the same time permit the binding of sterols at the deep 7TM site. Although many 7TM proteins are regulated by cholesterol, SMO uniquely contains two distinct sites that bind sterols, which suggests that there is a deep evolutionary link between SMO function and sterol biology. An important future challenge is to understand how SMO integrates the information relayed through each of these sterol-binding sites to ensure appropriate levels of Hh pathway activity in vivo. The existence of a deep 7TM sterol site and the presence of a potential conduit from the inner leaflet provide a connection between the cholesterol transporter-like activity of PTCH1 and the regulation of SMO, which sheds light on a long-standing puzzle in Hedgehog signalling in development, regeneration and cancer.

METHODS

No statistical methods were used to predetermine sample size. The experiments were not randomized and the investigators were not blinded to allocation during experiments and outcome assessment.

Expression and purification of SMO.

For nanobody generation, the wild-type mouse *Smo* gene, coding for residues 64 to 566, was cloned into a pVLAD6 vector containing an expression cassette with an HA signal sequence followed by a Flag epitope tag, a streptavidin binding peptide and tobacco etch virus (TEV) protease recognition sequence at the N terminus of SMO. To increase expression levels of wild-type SMO, the entire the alpha subunit of mouse G_o (GNAO) was fused to C terminus of SMO, preceded by a sortase recognition sequence and a rhinovirus 3C protease recognition site. A baculovirus was generated using *Spodoptera frugiperda* Sf9 insect cells (unauthenticated and untested for mycoplasma contamination, Expression Systems 94–001F) and the construct was expressed in HEK293S GnTI$^-$ cells (unauthenticated and untested for mycoplasma contamination, ATCC CRL-3022) using the BacMam approach[31] in the presence of 10 mM sodium butyrate. Cells were collected 24 h after transduction and stored at −80 °C until further use. Frozen cell pellets were thawed and washed with a hypotonic buffer (20 mM HEPES pH 7.5, 1 mM EDTA, supplemented with 0.02 mg/ml leupeptin and 160 μg/ml benzamidine) before solubilizing with 50 mM HEPES pH 7.5, 300 mM NaCl, 1% (w/v) *n*-dodecyl-β-D-maltopyranoside (DDM, Anatrace), 0.1% (w/v) cholesteryl hemisuccinate (CHS, Sigma), 5 mM $MgCl_2$, 20 mM KCl and 5 mM ATP for 1 h at 4 °C. Following centrifugation, the resulting supernatant was loaded on M1 anti-Flag antibody Sepharose beads and washed extensively in 50 mM HEPES pH 7.5, 300 mM NaCl, 0.1% DDM, 0.01% CHS, 5 mM $MgCl_2$, 20 mM KCl and 5 mM ATP. The glass column was capped with approximately 1 ml of wash buffer remaining and 200 μg of rhinovirus 3C protease was added to the resin. After incubation with the protease for 3 h at 4 °C, the resin was washed extensively and SMO was eluted with 50 mM HEPES pH 7.5, 150 mM NaCl, 0.1% DDM/0.01% CHS, 0.2 mg/ml Flag peptide and 5 mM EDTA. The protein was concentrated and the monomeric fraction was collected after size-exclusion chromatography over a Superdex S200 Increase 10/300 GL column (GE Healthcare) equilibrated with 20 mM HEPES pH 7.5, 150 mM NaCl and 0.1% DDM/0.01% CHS. Purified SMO was concentrated to 10 mg/ml using a Vivaspin 100-kDa MWCO concentrator and small aliquots were flash-frozen in liquid nitrogen and stored at −80 °C.

For two fluorophore yeast cell sorting, SMO was directly labelled by sortase conjugation of protein fluorophores appended with an N-terminal triglycine motif. Plasmids encoding an N-terminal GGG Clover[32] or TDsmURFP[33] were used to generate large quantities of each fluorophore. The SMO-$G\alpha_o$ was purified similar to the methods described above, but with an additional step to enable sortase-mediated conjugation of Clover or TDsmuRFP. Subsequent to lysis, solubilization and M1-Flag loading as described above, the column was capped with 1 ml of wash buffer. M1 beads were incubated with a large excess of either fluorescent protein (500 μM), 5 mM $CaCl_2$, 5 μM enhanced sortase[34] and 100 μg 3C protease at room temperature for 3 h. After extensive washing, the conjugated protein was eluted and further purified using size-exclusion chromatography as described above.

For crystallization, the wild-type mouse *Smo* gene, coding for residues 64 to 566, was cloned into a pVLAD6 vector containing an expression cassette with an HA signal sequence followed by a Flag epitope tag, and a TEV protease recognition site at the N terminus of SMO. This construct was also expressed in HEK293S GnTI$^-$ cells using the BacMam

approach in the presence of 10 mM sodium butyrate and 1 μM vismodegib (Advanced Chemblocks). Cells were collected 24 h after transduction and stored at −80 °C until further use. Frozen cell pellets were thawed and washed with a hypotonic buffer (20 mM HEPES pH 7.5, 1 μM EDTA, 1 μM vismodegib, supplemented with leupeptin and benzamidine) before solubilizing with 50 mM HEPES pH 7.5, 300 mM NaCl, 1% (w/v) DDM (Anatrace), 0.1% (w/v) CHS (Sigma), 1 μM vismodegib, 5 mM $MgCl_2$, 20 mM KCl and 5 mM ATP for 1 h at 4 °C. After high-speed centrifugation, the supernatant was subjected to affinity purification using an M1 anti-Flag antibody coupled to Sepharose beads. Extensive washes were done to ensure (1) detergent exchange from 1% DDM, 0.1% CHS to 0.01% (w/v) lauryl maltose neopentyl glycol (LMNG, Anatrace)/0.001% CHS; (2) ligand exchange from 1 μM vismodegib to 1 μM SAG21k (Tocris Bioscience); and (3) complete removal of ATP. Protein was eluted with 50 mM HEPES pH 7.5, 150 mM NaCl, 0.01% LMNG/0.001% CHS, 1 pM SAG21k, 0.2 mg/ml Flag peptide and 5 mM EDTA. Purified SMO was deglycosylated with endoglycosidase F1 and endoglycosidase H at room temperature for 30 min. SMO was then allowed to bind threefold molar excess purified NbSmo8 overnight at 4 °C. The following day, SMO-SAG21k-NbSmo8 complex was concentrated using a 50-kDa MWCO concentrator and loaded onto a Superdex 200 Increase 10/300 GL column (GE Healthcare) equilibrated with 20 mM HEPES pH 7.5, 150 mM NaCl, 0.1 pM SAG21k and 0.01% LMNG/0.001% CHS. Peak fractions corresponding to the protein complex were pooled, mixed with 10 μM SAG21k and concentrated to 50 mg/ml using a Vivaspin 100-kDa MWCO concentrator. Samples were aliquoted into thin-walled PCR tubes at 5 μl per aliquot. Aliquots were flash-frozen in liquid nitrogen and stored at −80 °C for crystallization experiments.

For fluorescence size-exclusion experiments, SMO was purified as above, but without inclusion of vismodegib during expression or purification. The SMO(V333F) mutant was expressed in Expi293 cells by transient transfection using the manufacturer's instructions, and purified without vismodegib. To make cholesterol directly available to SMO in biochemical experiments, the receptor was purified in complex with cholesterol-laden LMNG micelles. LMNG (500 mg) and cholesterol (3.9 mg) were dissolved in methanol followed by overnight vacuum-assisted evaporation of the solvent. The dried mixture was sonicated in 20 mM HEPES pH 7.5 to yield 5% (w/v) LMNG and 2 mol% cholesterol. SMO was expressed in HEK293S GnTI$^-$ cells as described above, solubilized and loaded onto M1-Flag, buffer-exchanged into LMNG-cholesterol micelles, eluted from M1-Flag and enzymatically deglycosylated as described above. Size-exclusion chromatography was performed in 20 mM HEPES pH 7.5, 150 mM NaCl and 0.01% (w/v) LMNG/2 mol% cholesterol. Peak fractions corresponding to SMO were pooled and concentrated to 32 mg/ml using a Vivaspin 100-kDa MWCO concentrator. Samples were stored at −80 °C until use.

Identification of NbSmo8.

Nanobodies against activated SMO were generated using a recently developed synthetic nanobody library[18]. For the first round of selection, yeast were selected with 1 μM purified SMO pre-complexed with 5 μM SAG21k. After incubation for 30 min at room temperature in selection buffer (20 mM HEPES pH 7.5, 150 mM NaCl, 0.1% DDM, 0.01% CHS, 1 μM

SAG21k, 0.5% w/v bovine serum albumin, 2 mM $CaCl_2$ and 10 mM maltose), yeast were washed twice with selection buffer and incubated with 10 μg/ml fluorescein-labelled anti-Flag M1 (M1-FITC) antibody for 15 min at room temperature. Subsequently, yeast were again washed and incubated for 15 min with anti-fluorescein microbeads (Miltenyi) at room temperature. Finally, yeast specific for SAG21k-occupied SMO were enriched by magnetic affinity cell sorting (MACS, Miltenyi). Recovered yeast were passaged in SDCAA medium and induced again in SGCAA medium, as previously described[18].

A second round of selection followed the same general template as the first round. However, before positive selection, a negative selection to deplete nanobodies that bind the Alexa647 fluorophore or M1 antibody was performed. Yeast were first incubated with 10 μg/ml Alexa647-labelled M1 antibody for 15 min at room temperature, then washed, incubated with anti-Cy5 microbeads and selected by MACS as above. Unbound yeast were subsequently positively selected with 1 μM SAG21k-SMO complex, as described for round 1. For identifying conformationally selective clones, a subsequent round of MACS was performed. Yeast were first incubated with 1 μM SMO pre-complexed with 5 μM KAAD-cyclopamine for 30 min at room temperature in selection buffer. After washing, yeast were incubated with 10 μg/ml M1-FITC for 15 min at room temperature, washed again and incubated with anti-fluorescein microbeads at room temperature. Yeast that did not bind to a magnetic column were collected, centrifuged, washed, resuspended in selection buffer and incubated with 1 μM SAG21k-SMO complex. The positive selection for SAG21k-SMO-specific yeast was performed as in the first round.

The final two rounds of selection used FACS with SMO directly conjugated to either Clover or TDsmURFP. Yeast were incubated simultaneously with 1 μM SAG21k-SMO-Clover and 1 μM KAAD-cyclopamine-SMO-TDsmURFP for 15 min at room temperature, then washed in ice-cold selection buffer. A small fraction of yeast (0.2% of total clones) with high signal in the FITC channel and low signal in the APC channel were isolated and expanded in SDCAA medium. After induction in SGCAA medium, another round of FACS was performed, switching the fluorophores conjugated to either agonist-or antagonist-bound SMO. Switching fluorophores eliminates yeast that directly binds the fluorophores. Yeast were incubated simultaneously with 1 μM SAG21k-SMO-TDsmURFP and 1 μM KAAD-cyclopamine-SMO-Clover for 15 min. The selection was performed as for the prior round of FACS, but yeast that uniquely stained positive for SAG21k-SMO-TDsmURFP in the APC channel were isolated. Collected yeast were grown in SDCAA medium. A yeast miniprep library was transformed into *Escherichia coli* and 17 unique clones were identified by Sanger sequencing. From these, 11 clones were confirmed to preferentially bind to only SAG21k-SMO and not KAAD-cyclopamine-SMO. For confirmation, individual nanobody clones were expressed on the yeast surface, stained with 1 μM SMO-SAG21k or 1 μM SMO-KAAD-cyclopamine, washed as above, stained with anti-Flag-Alexa647 and anti-HA-Alexa488 and analysed on a Becton Dickinson Accuri C6 flow cytometer.

Expression and purification of NbSmo8.

The sequence for NbSmo8 was amplified from the yeast surface display vector pYDS, and cloned into pET26b (Novagen) with a C-terminal hexahistidine tag. The construct was

transformed into BL21(DE3) Rosetta *E. coli,* grown in terrific broth medium supplemented with 2 mM $MgCl_2$ and 0.1% w/v glucose and induced at an optical density (OD) at 600 nm of 0.6 with 400 μM IPTG. After induction, cells were grown overnight at 20 °C and collected the following day. The bacterial pellet was resuspended in 5 ml of resuspension buffer (200 mM Tris pH 8.0, 500 mM sucrose, 0.5 mM EDTA and 0.1 mg of lysozyme) per gram of bacterial pellet. After stirring for 30 min at room temperature, two volumes of MilliQ water were added to induce hypotonic lysis of the periplasm and the solution was further stirred at room temperature for 45 min. The resulting lysate was supplemented with 150 mM NaCl, 5 mM $MgCl_2$ and 20 mM imidazole, before centrifugation at 30,000g for 25 min. at 4 °C. The supernatant was loaded over Ni-NTA resin, washed extensively with 20 mM HEPES pH 7.5, 500 mM NaCl and 20 mM imidazole, and eluted in the same buffer with 300 mM imidazole. Fractions were pooled and dialysed overnight in 20 mM HEPES pH 7.5, 300 mM NaCl at room temperature, concentrated and purified further by size-exclusion chromatography. Purified NbSmo8 was concentrated to 20–30 mg/ml, flash-frozen in small aliquots in liquid nitrogen and stored at −80 °C until further use.

Fluorescence size-exclusion chromatography.

To biochemically assess conformational specificity of NbSmo8, purified NbSmo8 was labelled with Alexa647 NHS ester (Pierce). The labelling reaction was done using 50 μM NbSmo8 and 200 μM Alexa647 NHS ester and incubated overnight at room temperature. After quenching with 100 mM Tris pH 7.5, NbSmo8 was dialysed extensively in 20 mM HEPES pH 7.5 and 150 mM NaCl. Fluorescence size-exclusion experiments used 0.9 μM SMO in 20 mM HEPES, 150 mM NaCl, 0.01% LMNG, doped with either 0.001% CHS or 2 mol% cholesterol and 2.0 μM NbSmo8-Alexa647. Ligands at 25 μM (SAG21k and SANT-1) were incubated with SMO for at least one hour before further incubation with NbSmo8-Alexa647 at room temperature for 30 min. For BODIPY-cyclopamine experiments, 0.5 μM SMO was incubated with 2.5 μM BODIPY-cyclopamine for 15 min before size-exclusion chromatography. Samples were loaded onto a Superdex S200 Increase 10/300 GL column (GE Healthcare) and fluorescence signal was measured using an in-line Jasco FP1520.

Surface plasmon resonance.

Surface plasmon resonance experiments were conducted with a Biacore T200 at 25 °C. His-tagged NbSmo8 at 30 μg/ml was immobilized on a Series S sensor chip CM5 (GE) covalently coupled to an anti-His antibody (GE) at an R_{max} of 57.7 resonance units (RU) upon binding. Irrelevant Nb39, specific for the μ-opioid receptor[35], was immobilized with an RU value that matched that of the reference surface, as a control for nonspecific binding. Measurements were made using four twofold serial dilutions of 1 μM SMO saturated with 10 μM SAG21k or SANT-1 or co-purified with cholesterol-laden LMNG micelles in a buffer containing 20 mM HEPES pH 7.5, 150 mM NaCl and 0.05% LMNG using single-cycle kinetics. All data were analysed with the Biacore T200 evaluation software version 2.0. Initial fits with a simple 1:1 Langmuir binding model showed reasonable fits with small residuals and low fit χ^2 values well within the manufacturer's described limits. Slightly improved fits were obtained using a two-state reaction model, which probably results from the conversion of SMO to a fully active SMO upon binding surface-immobilized NbSmo8.

Given the small overall improvement in fit quality with the more-paramterized two-state model, the simpler 1:1 model values are presented.

Fluorescence microscopy.

Two isogenic HEK293 Flp-in Trex cells (unauthenticated and untested for mycoplasma contamination; parental cell line from Thermo Fisher) were constructed for these experiments. For experiments involving SMO and NbSmo8 coexpression, an expression plasmid was engineered to contain an N-terminal streptavidin-binding-peptide-and Flag-tagged SMO truncated at residue 566[10], an IRES element and a NbSmo8-GFP fusion, all in the pCDNA5/FRT/ TO vector. For experiments involving SMO, PTCH1 and NbSmo8-GFP coexpression, we inserted into the construct described above a P2A peptide and a stabilized PTCH1 variant[12] between the end of SMO and the start of NbSmo8, allowing for tandem expression of all three proteins. Stable HEK293 Flp-in Trex cell lines were constructed according to the manufacturer's instructions and selected with blas-ticidin and hygromycin. Stably transfected cells were re-plated on poly-D-lysine-coated coverslips, and stimulated with various pharmacological agents for 1 h at the following concentrations: SAG21k (0.3 μM), KAAD-cyclopamine (0.3 μM) or methyl-β-cyclodextrin (4 mM). For MβCD cholesterol depletion experiments, mevastatin was also included at 8 μM to block de novo cholesterol biosynthesis. Live cells were subsequently stained for 5 min with an Alexa647-conjugated M1 Flag antibody, followed by washing, mounting and visualization. Images were acquired on a Leica SP8 laser scanning confocal microscope. Line scan analysis was performed using ImageJ software. Within each experiment, all images were acquired with identical gain and exposure settings and processed identically in ImageJ. Cells displaying unequivocal SMO staining at the membrane were taken for further analysis, and colocalization at the cell surface (defined as cells in which >60% of the perimeter was encircled by a ring of NbSmo8 overlapped with the Flag signal) was quantified across multiple fields.

SMO activity dependent immunoprecipitation of NbSmo8.

Suspension HEK293 cells (unauthenticated and untested for mycoplasma contamination; Thermo Fisher) were infected with BacMam viruses encoding an N-terminal streptavidin-binding-peptide-and Flag-tagged SMO truncated at residue 566 and fused to GNAO[10] along with either control Nb80-GFP, which is specific to the β2-adrenergic receptor, or NbSmo8-GFP fusions at a 1:1 ratio of SMO:Nb viruses. Sodium butyrate was added to 10 mM to enhance expression. After 24 h, cells were collected, washed once in Hank's Balanced Saline Solution, and incubated with DMSO vehicle or the following pharmacological agents at 37 °C for 90 min: KAAD-cyclopamine (1 μM), SAG2lk (1 μM) or MβCD (8 mM). Cells were lysed for 1 h in a buffer containing: 20 mM HEPES pH 7.5, 150 mM NaCl, 0.5% LMNG, 0.05% CHS, 100 μM TCEP, 1 mM $CaCl_2$ and complete protease inhibitors (Roche). Following centrifugation (20,000g, 4 °C, 20 min), a portion of the clarified lysate was saved as 'input, and the remainder incubated with M1 Flag affinity resin for 1 h at 4 °C with rotation. Resin was washed three times with wash buffer: 20 mM HEPES pH 7.5, 150 mM NaCl, 0.01% LMNG, 0.001% CHS, 100 μM TCEP and 1mM $CaCl_2$. Protein was eluted using the same buffer supplemented with 5 mM EDTA and 0.2 mg/ml Flag peptide (GenScript). SDS-PAGE on Criterion Stain-Free 4–20% TGX gels and immunoblotting was

done as previously described[10], using the following primary antibodies: mouse anti-Flag M1 (1:5,000), rabbit anti-GFP (1:5,000, Thermo Fisher) diluted into TBS + 0.1% Tween-20 + 1 mM $CaCl_2$. After washing and incubating with HRP-conjugated secondary antibodies (Promega), PVDF membranes were visualized on a ChemiDoc XRS+ system (BioRad). Uncropped images are presented in Supplementary Fig. 1.

Crystallization of SMO-SAG21k-NbSmo8 complex.

SMO-SAG21k-NbSmo8 at 50 mg/ml was reconstituted into lipidic cubic phase by mixing with molten lipid (90% 9.9 monoacylglycerol, 10% cholesterol) at a ratio of 2:3 (protein:lipid) using the twin-syringe method[36]. A GryphonLCP robot (Art Robbins Instruments) was used to dispense 30-nl boluses of protein laden mesophase overlaid with 600 nl of precipitant solution. Crystals were grown in 96-well glass sandwich plates at 4°C and 20 °C. Crystals used for data collection were grown in 0.1M MES pH 6.0, 22% (v/v) PEG300, 0.1 M ammonium phosphate dibasic and 1.5% (v/v) 1,2,3-heptanetriol at 4 °C for 10 days, and then moved to 20°C for another 10 days. Boluses containing crystals were then collected using mesh grid loops (MiTeGen) and flash-frozen in liquid nitrogen for data collection.

X-ray data collection, model building and refinement.

X-ray diffraction data were collected at the 23-ID-B and 23-ID-D beamlines (GM/CA) at the Advanced Photon Source, Argonne. Diffracting crystals were identified by rastering with an unattenuated 80 × 30-μm beam and 0.5-s exposure. Wedges of 10–40° were collected on many individual crystals using a 10 × 10-μm unattenuated beam with 0.2-s exposure and 0.5°-oscillation. Diffraction data from the 20 best diffracting crystals were processed using XDS[37]. The structure was solved using molecular replacement with the program PHASER[38] using the structure of hSMO (PDB code 5L7D[7], lacking BRIL fusion and TM5 and TM6) and Nb6B9 (PDB code 4LDE[39], lacking complementarity determining regions (CDRs)) as two independent search models. The resulting structure was iteratively refined using Phenix[40] and BUSTER, and manually rebuilt in Coot[41]. Data collection and refinement statistics are summarized in Extended Data Table 1. The final model contained 95.17%, 4.83% and 0% in the favoured, allowed and outlier regions of the Ramachandran plot, respectively. Structure figures were prepared in PyMol (Schrödinger).

Molecular dynamics simulations.

System setup for molecular dynamics simulations.—We prepared two separate simulation conditions to probe the stability of the 7TM cholesterol in two different orientations. For both conditions, we removed the SAG21k agonist as well as NbSmo8. The first condition contained cholesterol with its hydroxyl group oriented towards the intracellular side. The second condition was initiated from a slightly refined model, with its hydroxyl group oriented towards the extracellular side. Both models are available upon request. Before running molecular dynamics simulations of SMO, we performed several steps of refinement and modelling of the crystal structure. Prime (Schrödinger) was used to model in missing residue side chains, and neutral and methylamide groups were added to cap the protein termini. Histidine residues 231, 365 and 474 were represented with the

hydrogen on the delta nitrogen, and all other histidine residues were represented with the hydrogen on the epsilon nitrogen. In the first condition, Glu185 was protonated, as its pK_a value was predicted to be greater than 7.00; in the second condition, this residue was left charged (consistent with its predicted pK_a). For both conditions, Glu522 was protonated. All other residues were left at their default protonation state at pH 7.0. Each of the prepared systems was inserted into a pre-equilibrated palmitoyl oleoylphosphatidylcholine bilayer using Dabble[42]. We performed 6 independent simulations of each condition; each simulation was 0.6–1.2 μs in length, for a total of about 5.0 μs of aggregate simulation per condition. A table describing all simulations performed is provided in Supplementary Information Table 2.

Molecular dynamics simulation force-field parameters.—The CHARMM36m parameters were applied to protein, CHARMM36 parameters to lipids, salt and the N-acetyl glucosamine modification and the CHARMM36 TIP3P parameter set to water[43–46].

Molecular dynamics simulation protocol.—Molecular dynamics simulations were performed on GPUs with the CUDA-enabled version of PMEMD in AMBER16[47,48]. Each simulation underwent a similar equilibration procedure. Following an initial minimization, each system was heated with a Langevin thermostat from 0 to 100 K in the NVT ensemble over 12.5 ps with 10 kcal mol^{-1} Å^{-2} harmonic restraints on all non-hydrogen atoms in the protein, ligand and lipid. Heating continued in the NPT ensemble with semi-isotropic coupling for 125 ps and a pressure of 1 bar to a final temperature of 310 K with 5.0 kcal mol^{-1} Å^{-2} harmonic restraints. Further equilibration was then carried out at 310 K with harmonic restraints applied to the protein starting at 5.0 kcal mol^{-1} Å^{-2} and reduced in a stepwise fashion every 2 ns for 10 ns, followed by 0.1 kcal mol^{-1} Å^{-2} restraints for 20 ns for a total of 28 ns of restrained equilibration. Production simulations were run at 310 K and 1 bar in the NPT ensemble using the Langevin thermostat and Monte Carlo barostat.

Each simulation used periodic boundaries and used a time step of 4.0 fs using hydrogen-mass repartioning[49]. All bond lengths to hydrogens were constrained by SHAKE[50]. Short-range electrostatic and van der Waals interactions were cut off at 9.0 Å, whereas long-range electrostatic interactions were computed using the particle mesh Ewald method. The fast Fourier transform grid size was chosen such that the width of a single grid cell was approximately 1 Å.

Snapshots from each trajectory were saved every 200 ps during the production phase of each simulation, and visualized using VMD[51]. Analysis was carried out using a combination of VMD, cpptraj[52] and analysis tools developed in-house. For histogram generation in Extended Data Fig. 5, we removed the first 100 ns to allow for simulation convergence. To quantify the outward displacement of the intracellular end of TM6 relative to TM1, we projected a vector defined by the displacement of TM6 (Cα D259) in simulation from the crystallographic posi-tion of TM1 (Cα K448) onto the vector defined by the displacement of the same two atoms in the crystal structure. We then report the position of the TM6 point projected onto this second vector, with values greater than the crystallographic extent of TM6 displacement (21.3 Å) indicating outward displacement of TM6. We performed this

analysis on every simulation frame after aligning all simula-tion frames to the initial structure, using helical segments of the transmembrane domain for alignment.

SMO signalling studies.

Maintenance and transfection of 4C20 *Smo*$^{-/-}$ mouse embryonic fibroblasts as well as GLI-luciferase reporter assays were performed as previously described[11]. In brief, 4C20 *Smo*$^{-/-}$ cells (authenticated by presence of genomic knockout by PCR and absence of SMO protein by western blot and peri-odically tested for mycoplasma contamination; from the P. A. Beachy laboratory) were seeded into 24-well plates and transfected with various plasmids along with a mixture of 8×GLI-luciferase and SV40-Renilla plasmids using TransIT 2020 transfection reagents (Mirus), following manufacturer's instructions. For each well, 2.5 ng of *Smo* cDNA, 125 ng 8×GLI-luciferase plasmid, 5 ng SV40-Renilla plasmid and 120 ng GFP expression plasmid were used for transfection. After the cells grew to confluency, the medium was replaced with DMEM containing 0.5% serum and various drugs or vehicle control. Cholesterol–MβCD inclusion complexes were prepared as previously described[53]. In brief, a 1:10 molar ratio of cholesterol:MβCD was prepared by adding 9% (w/v) MβCD (Sigma 332615, lot no. STBC2412V, 1.6–2.0 mol CH_3 per unit anhydroglucose) to dried cholesterol, heating to 80 °C and sonicating until a clear solution was achieved. Luciferase activity was measured after 48 h of drug treatment using the Dual luciferase assay kit (Promega) on a Berthold Centro XS3 luminometer.

BODIPY-cyclopamine binding studies.

Freestyle 293 cells were transfected in 12-well plates with the described expression vectors (1 μg per well) and, after 2 days, incubated in Freestyle-293 medium (Thermo Fisher) containing 1% fetal bovine serum, 5 nM BODIPY-cyclopamine (Toronto Research Chemicals) and various concentrations of KAAD-cyclopamine (Toronto Research Chemicals) at 37 °C for 3–4 h. The cells were then washed with phosphate buffered saline and resuspended in fresh medium for flow cytometry experiments. The percentage of cells positive for BODIPY-cyclopamine fluorescence was quantified by flow cytometry on a BD FACSAria II.

Reporting summary.

Further information on research design is available in the Nature Research Reporting Summary linked to this paper.

Extended Data

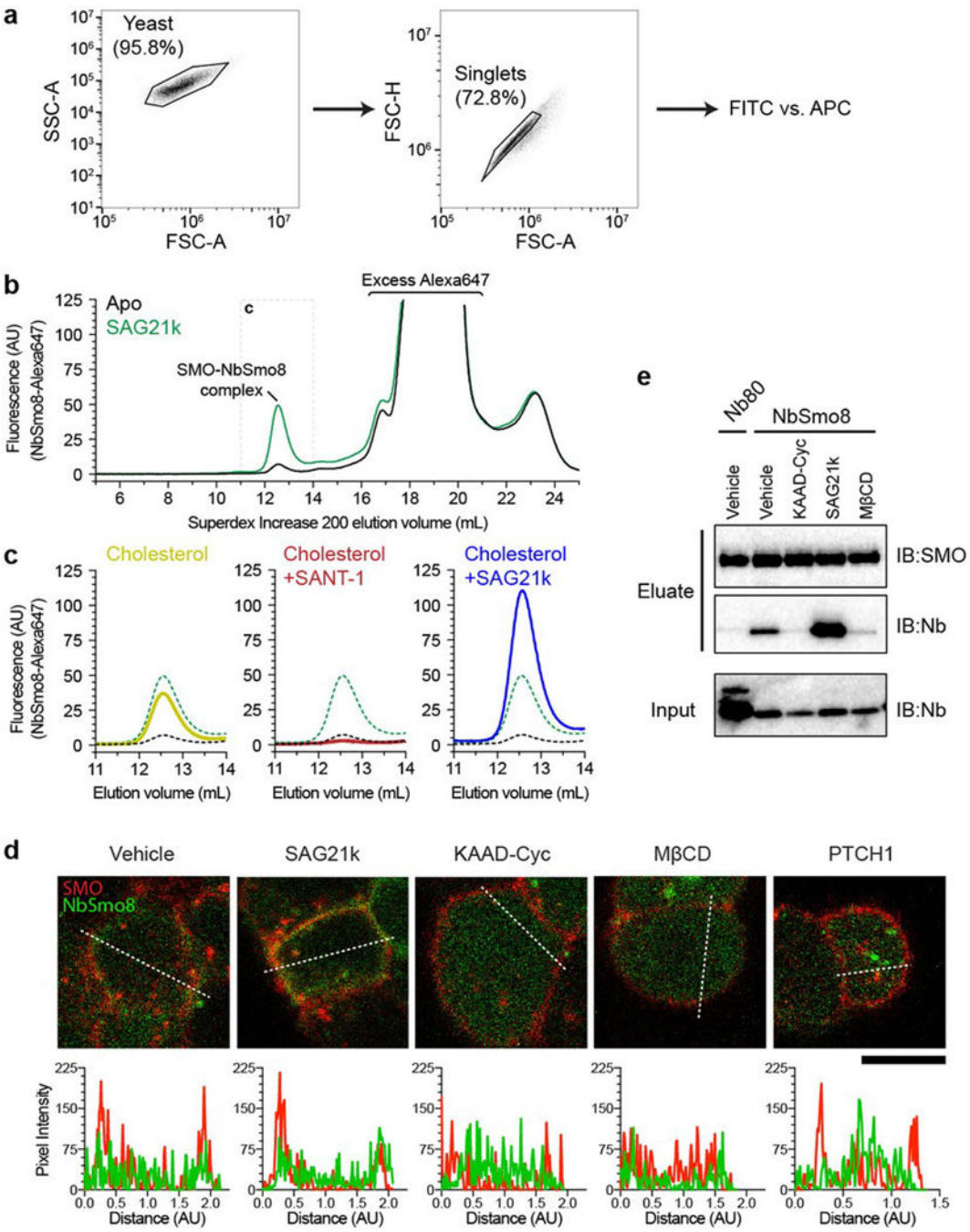

Extended Data Fig. 1 |. NbSmo8 is selective for active SMO.

a, Gating scheme for flow cytometry experiments in Fig. 1b with selection of yeast singlets for analysis. **b**, Fluorescent size-exclusion chromatography traces of 2 μM NbSmo8–Alexa647 incubated with 0.9 μM SMO incubated with or without 25 μ M SAG21k. NbSmo8 co-elutes with SMO–SAG21k with an elution volume of 12.5 ml. **c**, Fluorescent size-exclusion chromatography traces of NbSmo8–Alexa647 as in **b**, with SMO purified in the presence of cholesterol–LMNG micelles (yellow). Dashed traces depict apo (black) and SAG21k (green) conditions shown in **b**. Cholesterol potentiates NbSmo8 binding. SANT-1

(25 μM) (red) completely prevents NbSmo8 binding. SAG21k is cooperative with cholesterol and increases NbSmo8 binding (blue). **d**, Representative line scans (pixel intensity versus distance, both in arbitrary units) for cells in Fig. 1d. Dashed white line indicates the location of the scan. Scale bar, 10 μm. **e**, Co-immunoprecipitation of NbSmo8 is dependent on SMO activation. Flag–SMO was co-expressed in suspension HEK293 cells with GFP-tagged versions of NbSmo8 or Nb80, a control nanobody specific to the β_2-adrenergic receptor with no affinity for SMO. After stimulation with DMSO (vehicle), KAAD-cyclopamine (KAAD-cyc), SAG21k or MβCD, cells were solubilized in LMNG and SMO–nanobody complexes were isolated using M1 Flag affinity resin. SMO (anti-Flag antibody) and NbSmo8 or Nb80 (anti-GFP antibody) were evaluated via immunoblotting.

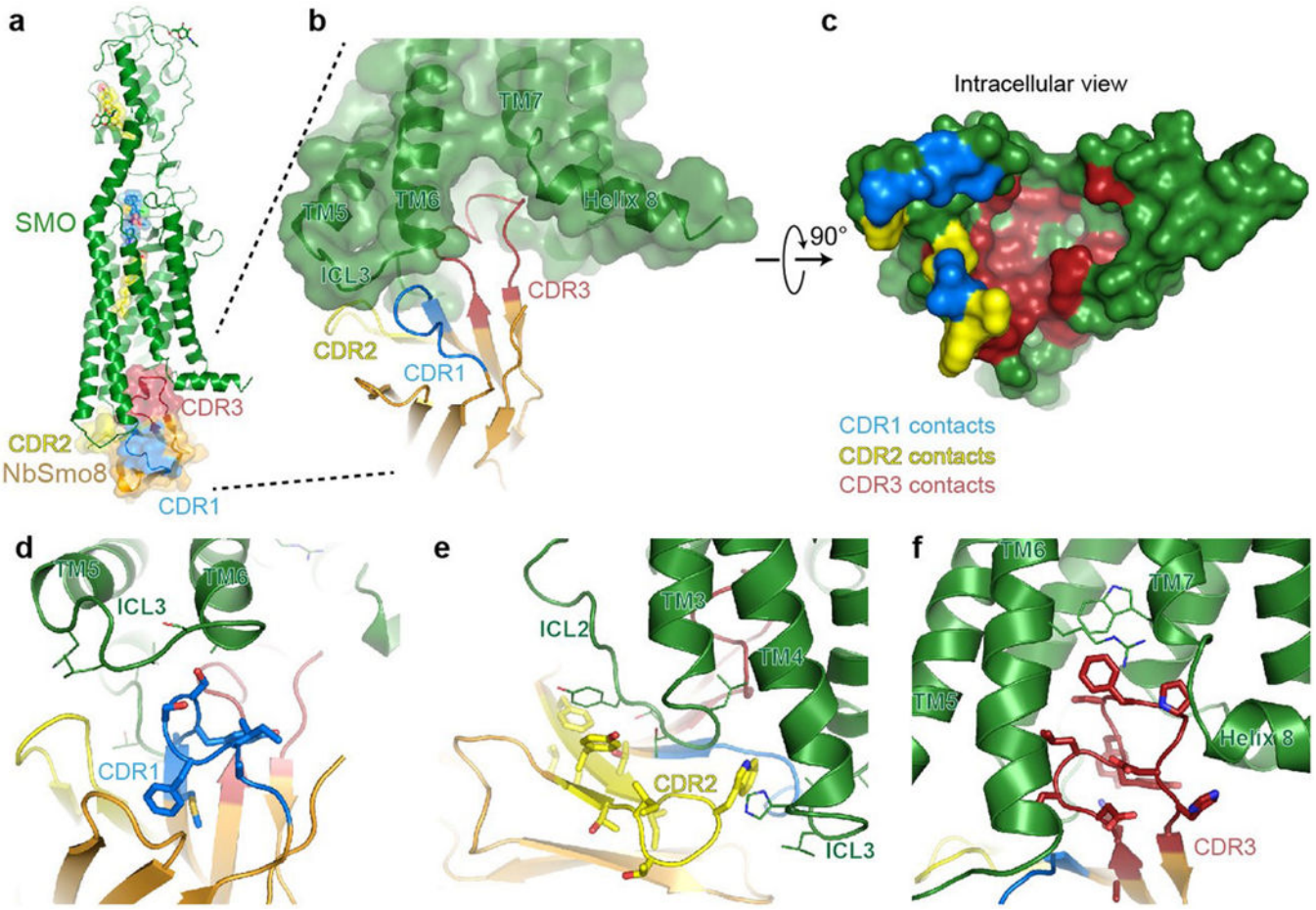

Extended Data Fig. 2 |. NbSmo8 recognition of active SMO.

a, Overall structure of active SMO bound to NbSmo8. The three highly variable nanobody CDRs are highlighted in different colours. **b**, Close-up view of the interface. NbSmo8 CDRs recognize a large intracellular cavity in active SMO. **c**, Intracellular view of active SMO cavity stabilized by NbSmo8. Surface is coloured by regions that are contacted by a specific NbSmo8 CDR. NbSmo8 recognizes a unique three-dimensional epitope, with each CDR making important contributions to overall binding. **d**, CDR1 makes important contacts with SMO intracellular loop (ICL) 3. **e**, CDR2 residues interact with ICL2 and ICL3. **f**, The long CDR3 has a complex fold that reaches deep inside the active SMO cavity and stabilizes an outwardly displaced conformation of TM6.

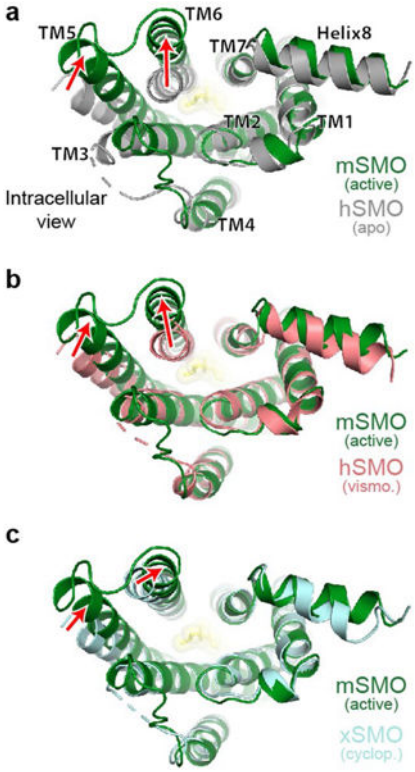

Extended Data Fig. 3 |. Activation-induced changes in SMO.

a–**c**, Cytoplasmic view of 7TM helix rearrangements of active SMO–SAG21k–NbSmo8 (green) compared with apo hSMO (PDB code 5L7D) (grey) (**a**), inactive hSMO (PDB code 5L7I) (salmon) (**b**) and intermediate active xSMO (PDB code 6D32) (cyan) (**c**). In all panels, the TM6 outward movement and TM5 inward movement are highlighted with a red arrow.

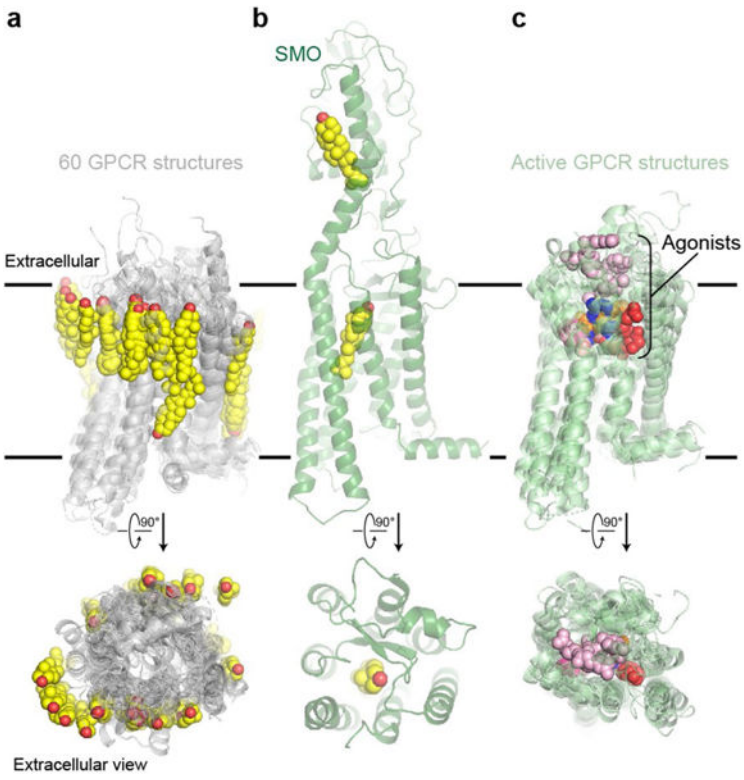

Extended Data Fig. 4 |. Unique binding mode of 7TM cholesterol.

a, All experimentally determined GPCR structures in the PDB with a modelled cholesterol (60 individual structures) are shown overlaid with receptors shown in light grey. In each case, cholesterol binds outside of the 7TM bundle. **b**, **c**, By contrast, the 7TM cholesterol in active SMO binds within the 7TM bundle (**b**), which is highly similar to the binding mode of agonists bound to active GPCRs (**c**) (eight individual structures; agonists are shown in unique colours, and GPCRs in light green transparency).

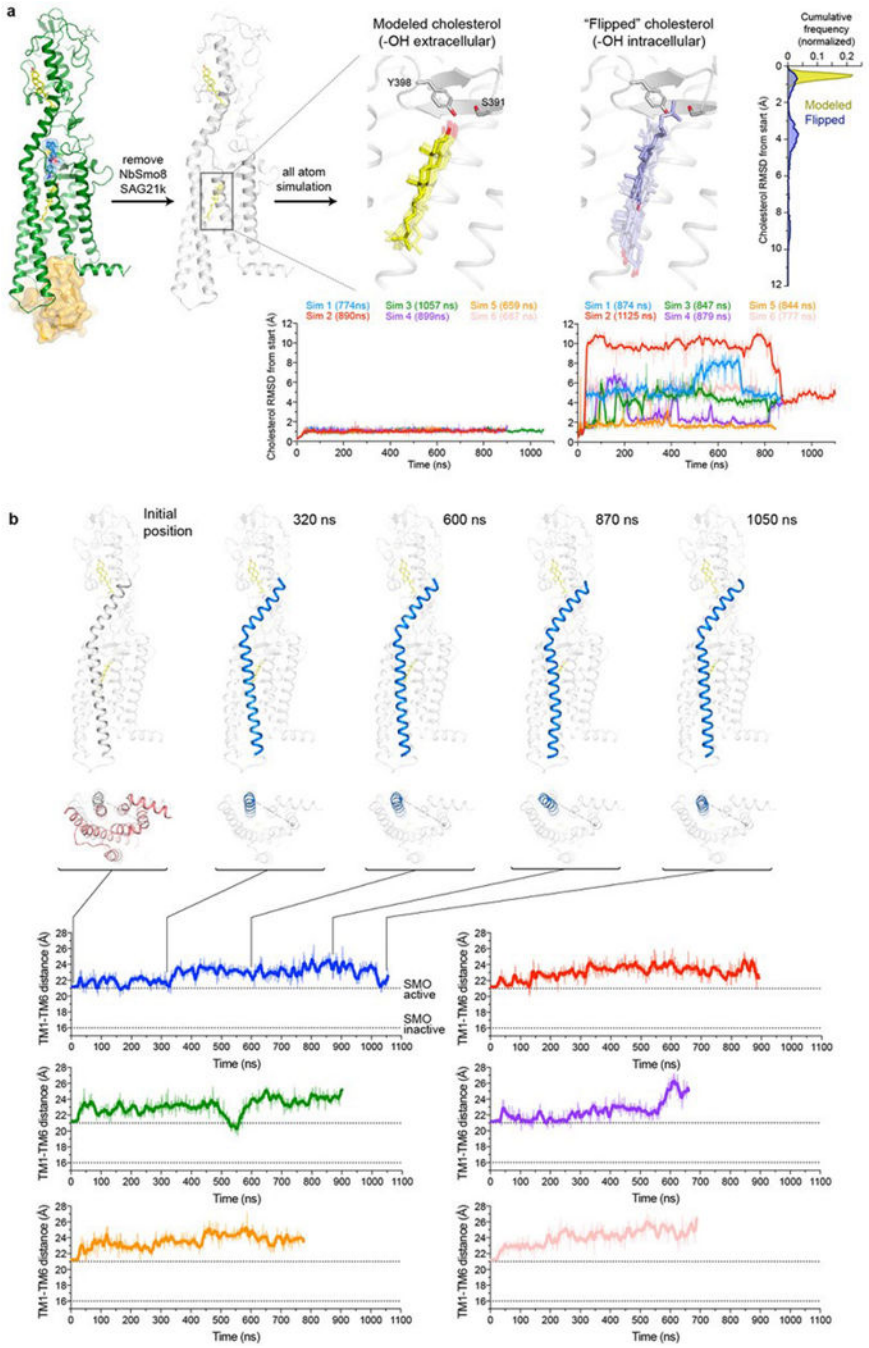

Extended Data Fig. 5 |. Molecular dynamics of active SMO.

All atom molecular dynamics simulations of SMO were performed in the absence of SAG21k and NbSmo8 to assess the stability of 7TM cholesterol and the overall stability of the active conformation. **a**, A model of active SMO derived from lower-resolution data had initially placed cholesterol in an opposite ‘flipped’ orientation (right panel and graph), with the hydroxyl pointing towards the intracellular side. In five out of six simulations starting from such a pose, cholesterol displayed substantial movement deeper into the 7TM pocket. By contrast, the correctly modelled cholesterol (left panel and graph) was stable over all six

simulations, showing an overall root mean squared deviation of 1 Å from the starting position. Close-up view of the binding pockets shows simulation frames sampled every 50 ns from a representative simulation as transparent sticks. **b**, Even after removal of NbSmo8 and SAG21k, TM6 remains close to its initial position but can adopt slightly outward conformations. The displacement of Cα D259 in TM6 from Cα K448 in TM1 is used to track TM6 movement (Methods); these atoms are shown as spheres. Individual structural snapshots from a representative simulation are shown with the conformation of TM6 highlighted in blue. For comparison, the structure of inactive SMO is shown in the intracellular view (salmon cartoon). TM6 spontaneously returns to the crystallographic conformation after outward displacements, which provides confidence in the observed state stabilized by NbSmo8.

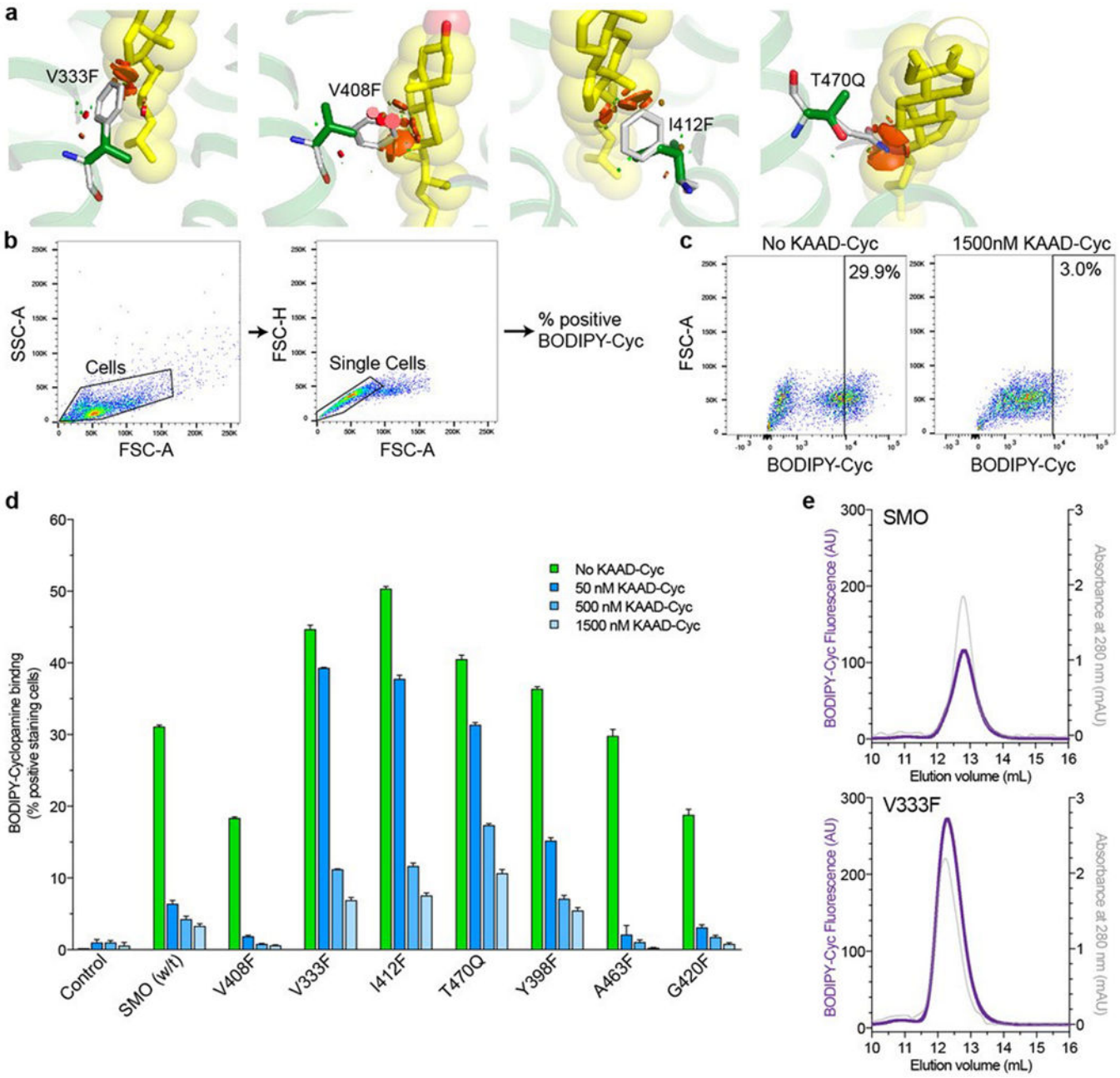

Extended Data Fig. 6 |. SMO mutants bind BODIPY-cyclopamine.

a, Structural modelling of SMO mutations that line the deep 7TM sterol pocket. Wild-type residues are shown as green sticks. Grey sticks show the most -common rotamer of each engineered mutation that does not clash with neighbouring residues in SMO. Red regions show clashes between engineered mutations and cholesterol. **b**, Gating scheme for BODIPY-cyclopamine (BODIPY-cyc) binding flow cytometry experiments with selection of single cells for analysis. **c**, Example of flow cytometry plots showing percentage of BODIPY-cyclopamine^{+} cells with and without competition with KAAD-cyclopamine. Plots shown are for cells that express wild-type SMO. **d**, Engineered mutations in SMO used to probe the 7TM sterol site and the hydrophobic tunnel are fully competent to bind BODIPY-

cyclopamine, which indicates that these mutations fold and traffic to the cellular membrane. Some mutants (including V333F, I412F and T470Q) show increased BODIPY-cyclopamine binding compared to wild-type SMO, which suggests that they stabilize the inactive conformation. Mean ± s.e.m., $n = 3$ biological replicates. **e**, Fluorescence size-exclusion chromatography traces of 0.5 μM SMO and SMO(V333F) incubated with 2.5 μM BODIPY-cyclopamine. Both preparations bind BODIPY-cyclopamine, which indicates that the purified proteins are functionally capable of binding ligands.

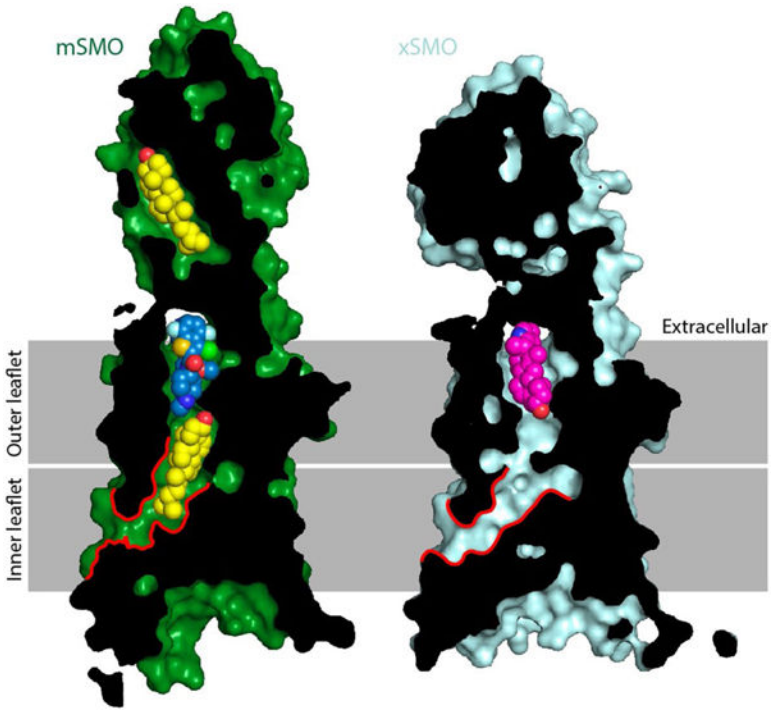

Extended Data Fig. 7 |. Comparison of hydrophobic tunnel in mSMO and xSMO.
Cutaway view of active mSMO (green surface) and cyclopamine-bound xSMO (PDB code 6D32) (cyan surface) in similar orientations. In both cases, a hydrophobic tunnel opening to the inner leaflet of the plasma membrane is observed (outlined in red).

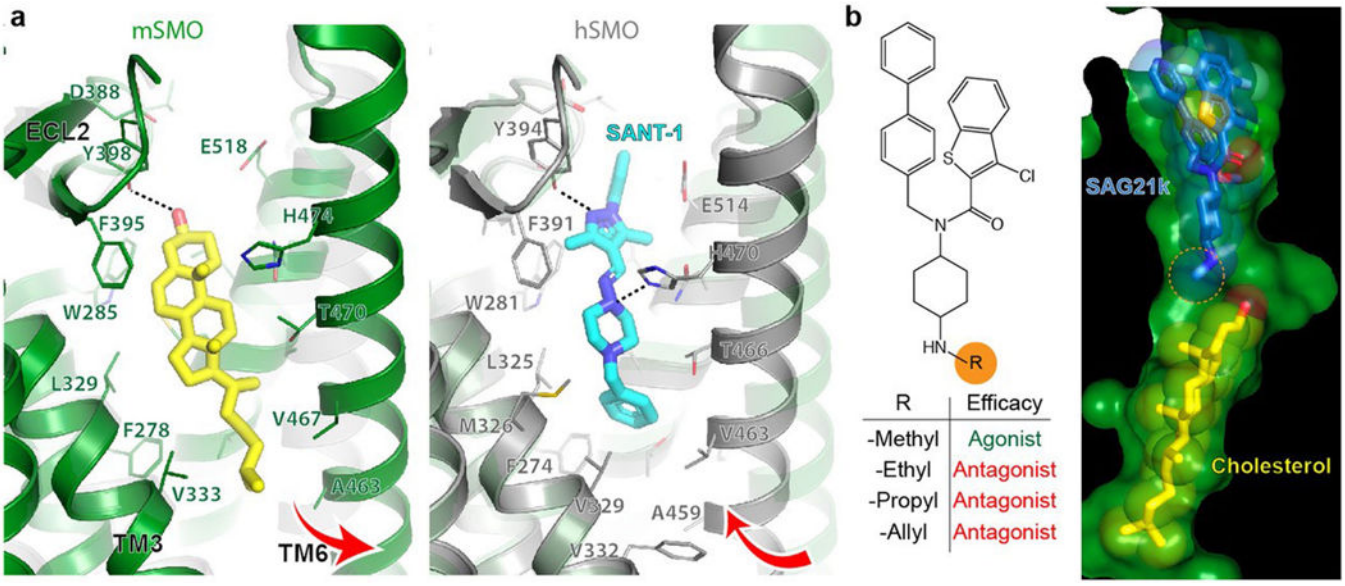

Extended Data Fig. 8 |. SMO structural pharmacology at the 7TM site.

a, Comparison of cholesterol bound to active SMO (green cartoon) and SANT-1 bound to inactive SMO (PDB code 4N4W) (grey cartoon). A hydrogen bond between H470 of hSMO (H474 of mSMO) and SANT-1 (dotted black line) stabilizes an inward conformation of TM6. By comparison, the bulky cholesterol methyl groups outwardly displace TM6. Both cholesterol and SANT-1 form a hydrogen bond with Y398. **b**, Structure–activity relationship of SAG (adapted from ref. [27]). Bulkier replacements to the 4-amino group (orange circle) that are predicted to clash with the 7TM cholesterol switch the molecular efficacy of SAG from an agonist into an antagonist.

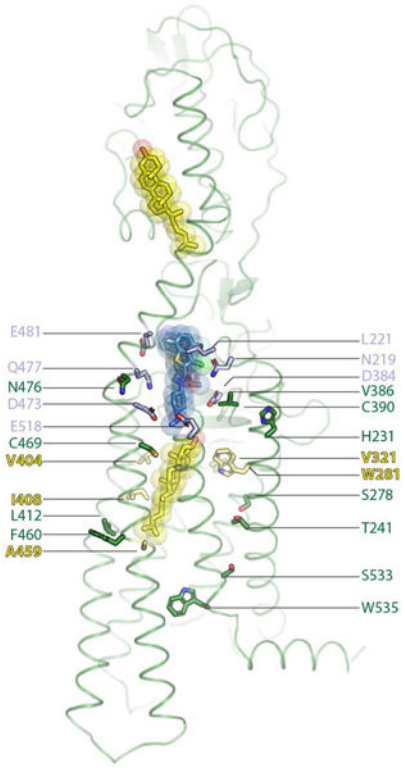

Extended Data Fig. 9 |. SMO-inhibitor resistance mutations.
Previously identified[54–58] hSMO-inhibitor resistance mutations are shown as sticks mapped onto the active mSMO structure. Numbering is for hSMO. Residues highlighted in light violet are within 5 Å of SAG21k. Mutations in this upper site probably directly disrupt inhibitor binding. Residues in yellow are within 5 Å of the 7TM cholesterol. Mutations in these sites probably alter sterol affinity or directly stabilize the active SMO conformation. Residues in green are outside of the 7TM binding pocket and probably stabilize the SMO active state.

Extended Data Table 1 |

Data collection and refinement statistics (molecular replacement)

	SMO-S AG21 k-Cholesterol-NbSmo8[a]
Data collection	
Space group	$P222_1$
Cell dimensions	
a, *b*, *c* (Å)	39.01, 121.09, 157.01
α, β, γ (°)	90.0, 90.0, 90.0
Resolution (Å)	40.36 – 2.80 (2.90 – 2.80)[b]
R_{sym} Or R_{merge}	0.27 (1.87)
$I/\sigma I$	5.48 (0.92)
Completeness (%)	96.2 (94.0)

	SMO-S AG21 k-Cholesterol-NbSmo8[a]
Redundancy	6.6 (3.5)
CC (1/2) (%)	99.2 (23.0)
Refinement	
Resolution (Å)	40.36 – 2.80
No. reflections	18462
R_{work} / R_{free} (%)	24.5 / 29.4
No. atoms	
Protein	4676
Ligand/ion	95
Water	3
B-factors	
Protein	74.34
Ligand/ion	70.79
Water	67.38
R.m.s. deviations	
Bond lengths (Å)	0.004
Bond angles (°)	0.49

[a]Data merged from 20 crystals.

[b]Values in parentheses are for highest-resolution shell.

Supplementary Material

Refer to Web version on PubMed Central for supplementary material.

Acknowledgements

This work was supported by National Institutes of Health (NIH) grants DP50D023048 (A.M.), R01GM127359 (R.O.D.) and R01GM102498 (P.A.B.). I.D. acknowledges support from the Swiss National Science Foundation. A.M. acknowledges support from the Pew Charitable Trusts. B.R.M. acknowledges support from the American Cancer Society. N.R.L. and K.J.R. were supported by National Science Foundation Graduate Research Fellowships and K.J.R. by a Gerhard Casper Stanford Graduate Fellowship.

The content is solely the responsibility of the authors and does not necessarily represent the official view of the NIH. We thank A. Wang for assistance with simulation setup and analysis. We thank the staff at the GM/CA beamlines at the Advanced Photon Source, which have been funded in whole or in part with federal funds from the National Cancer Institute (ACB-12002) and the National Institute of General Medical Sciences (AGM-12006). This research used resources of the Advanced Photon Source, a US Department of Energy (DOE) Office of Science User Facility operated for the DOE Office of Science by Argonne National Laboratory under Contract No. DE-AC02–06CH11357. The Eiger 16M detector was funded by an NIH-Office of Research Infrastructure Programs, High-End Instrumentation Grant (1S10OD012289–01A1).

References

1. Briscoe J & Thérond PP The mechanisms of Hedgehog signalling and its roles in development and disease. Nat. Rev. Mol. Cell Biol. 14, 416–429 (2013). [PubMed: 23719536]
2. Wu F, Zhang Y, Sun B, McMahon AP & Wang Y Hedgehog signaling: from basic biology to cancer therapy. Cell Chem. Biol. 24, 252–280 (2017). [PubMed: 28286127]
3. Huang P et al. Cellular cholesterol directly activates Smoothened in Hedgehog signaling. Cell 166, 1176–1187.e1114 (2016). [PubMed: 27545348]

4. Huang P et al. Structural basis of Smoothened activation in Hedgehog signaling. Cell 174, 312–324.e316 (2018). [PubMed: 29804838]
5. Byrne EF, Luchetti G, Rohatgi R & Siebold C Multiple ligand binding sites regulate the Hedgehog signal transducer Smoothened in vertebrates. Curr. Opin. Cell Biol. 51, 81–88 (2018). [PubMed: 29268141]
6. Taipale J, Cooper MK, Maiti T & Beachy PA Patched acts catalytically to suppress the activity of Smoothened. Nature 418, 892–896 (2002). [PubMed: 12192414]
7. Byrne E F X. et al. Structural basis of Smoothened regulation by its extracellular domains. Nature 535, 517–522 (2016). [PubMed: 27437577]
8. Cooper MK et al. A defective response to Hedgehog signaling in disorders of cholesterol biosynthesis. Nat. Genet. 33, 508–513 (2003). [PubMed: 12652302]
9. Luchetti G et al. Cholesterol activates the G-protein coupled receptor Smoothened to promote Hedgehog signaling. eLife 5, e20304 (2016).
10. Myers BR, Neahring L, Zhang Y, Roberts KJ & Beachy PA Rapid, direct activity assays for Smoothened reveal Hedgehog pathway regulation by membrane cholesterol and extracellular sodium. Proc. Natl Acad. Sci. USA 114, E11141–E11150 (2017).
11. Myers BR et al. Hedgehog pathway modulation by multiple lipid binding sites on the Smoothened effector of signal response. Dev. Cell 26, 346–357 (2013). [PubMed: 23954590]
12. Zhang Y et al. Structural basis for cholesterol transport-like activity of the Hedgehog receptor Patched. Cell 175, 1352–1364.e1314 (2018). [PubMed: 30415841]
13. Gong X et al. Structural basis for the recognition of Sonic Hedgehog by human Patched 1. Science 361, eaas8935 (2018).
14. Qi X, Schmiege P, Coutavas E, Wang J & Li X Structures of human Patched and its complex with native palmitoylated sonic hedgehog. Nature 560, 128–132 (2018). [PubMed: 29995851]
15. Blassberg R, Macrae JI, Briscoe J & Jacob J Reduced cholesterol levels impair Smoothened activation in Smith-Lemli-Opitz syndrome. Hum. Mol. Genet. 25, 693–705 (2016). [PubMed: 26685159]
16. Manglik A, Kobilka BK & Steyaert J Nanobodies to study G protein-coupled receptor structure and function. Annu. Rev. Pharmacol. Toxicol. 57, 19–37 (2017). [PubMed: 27959623]
17. Ayers KL & Thérond PP Evaluating Smoothened as a G-protein-coupled receptor for Hedgehog signalling. Trends Cell Biol. 20, 287–298 (2010). [PubMed: 20207148]
18. McMahon C et al. Yeast surface display platform for rapid discovery of conformationally selective nanobodies. Nat. Struct. Mol. Biol. 25, 289–296 (2018). [PubMed: 29434346]
19. Manglik A & Kruse AC Structural basis for G protein-coupled receptor activation. Biochemistry 56, 5628–5634 (2017). [PubMed: 28967738]
20. Zhang X et al. Crystal structure of a multi-domain human smoothened receptor in complex with a super stabilizing ligand. Nat. Commun. 8, 15383 (2017). [PubMed: 28513578]
21. Wang C et al. Structural basis for Smoothened receptor modulation and chemoresistance to anticancer drugs. Nat. Commun. 5, 4355 (2014). [PubMed: 25008467]
22. Chen JK, Taipale J, Cooper MK & Beachy PA Inhibition of Hedgehog signaling by direct binding of cyclopamine to Smoothened. Genes Dev. 16, 2743–2748 (2002). [PubMed: 12414725]
23. Rohatgi R, Milenkovic L, Corcoran RB & Scott MP Hedgehog signal transduction by Smoothened: pharmacologic evidence for a 2-step activation process. Proc. Natl Acad. Sci. USA 106, 3196–3201 (2009). [PubMed: 19218434]
24. Taipale J et al. Effects of oncogenic mutations in Smoothened and Patched can be reversed by cyclopamine. Nature 406, 1005–1009 (2000). [PubMed: 10984056]
25. Raleigh DR et al. Cilia-associated oxysterols activate Smoothened. Mol. Cell 72, 316–327.e315 (2018). [PubMed: 30340023]
26. Audet M & Stevens RC Emerging structural biology of lipid G protein-coupled receptors. Protein Sci. 28, 292–304 (2019). [PubMed: 30239054]
27. Yang H et al. Converse conformational control of Smoothened activity by structurally related small molecules. J. Biol. Chem. 284, 20876–20884 (2009). [PubMed: 19366682]

28. Chen JK, Taipale J, Young KE, Maiti T & Beachy PA Small molecule modulation of Smoothened activity. Proc. Natl Acad. Sci. USA 99, 14071–14076 (2002). [PubMed: 12391318]
29. Nachtergaele S et al. Structure and function of the Smoothened extracellular domain in vertebrate Hedgehog signaling. eLife 2, e01340 (2013).
30. Nedelcu D, Liu J, Xu Y, Jao C & Salic A Oxysterol binding to the extracellular domain of Smoothened in Hedgehog signaling. Nat. Chem. Biol. 9, 557–564 (2013). [PubMed: 23831757]
31. Goehring A et al. Screening and large-scale expression of membrane proteins in mammalian cells for structural studies. Nat. Protoc. 9, 2574–2585 (2014). [PubMed: 25299155]
32. Lam AJ et al. Improving FRET dynamic range with bright green and red fluorescent proteins. Nat. Methods 9, 1005–1012 (2012). [PubMed: 22961245]
33. Rodriguez EA et al. A far-red fluorescent protein evolved from a cyanobacterial phycobiliprotein. Nat. Methods 13, 763–769 (2016). [PubMed: 27479328]
34. Chen I, Dorr BM & Liu DR A general strategy for the evolution of bond-forming enzymes using yeast display. Proc. Natl Acad. Sci. USA 108, 11399–11404 (2011). [PubMed: 21697512]
35. Huang W et al. Structural insights into μ-opioid receptor activation. Nature 524, 315–321 (2015). [PubMed: 26245379]
36. Caffrey M & Cherezov V Crystallizing membrane proteins using lipidic mesophases. Nat. Protoc. 4, 706–731 (2009). [PubMed: 19390528]
37. Kabsch W Xds. Acta Crystallogr. D 66, 125–132 (2010). [PubMed: 20124692]
38. McCoy AJ et al. Phaser crystallographic software. J. Appl. Crystallogr. 40, 658–674 (2007). [PubMed: 19461840]
39. Ring AM et al. Adrenaline-activated structure of β2-adrenoceptor stabilized by an engineered nanobody. Nature 502, 575–579 (2013). [PubMed: 24056936]
40. Adams PD et al. PHENIX: a comprehensive Python-based system for macromolecular structure solution. Acta Crystallogr. D 66, 213–221 (2010). [PubMed: 20124702]
41. Emsley P, Lohkamp B, Scott WG & Cowtan K Features and development of Coot. Acta Crystallogr. D 66, 486–501 (2010). [PubMed: 20383002]
42. Betz R Dabble http://dabble.robinbetz.com/ (2017).
43. MacKerell AD et al. All-atom empirical potential for molecular modeling and dynamics studies of proteins. J. Phys. Chem. B 102, 3586–3616 (1998). [PubMed: 24889800]
44. MacKerell AD, Jr, Feig, M. & Brooks, C. L. III. Improved treatment of the protein backbone in empirical force fields. J. Am. Chem. Soc. 126, 698–699 (2004). [PubMed: 14733527]
45. Guvench O et al. CHARMM additive all-atom force field for carbohydrate derivatives and its utility in polysaccharide and carbohydrate-protein modeling. J. Chem. Theory Comput. 7, 3162–3180 (2011). [PubMed: 22125473]
46. Best RB et al. Optimization of the additive CHARMM all-atom protein force field targeting improved sampling of the backbone ϕ, ψ and side-chain χ1 and χ2 dihedral angles. J. Chem. Theory Comput. 8, 3257–3273 (2012). [PubMed: 23341755]
47. Salomon-Ferrer R, Götz AW, Poole D, Le Grand S & Walker RC Routine microsecond molecular dynamics simulations with AMBER on GPUs. 2. Explicit solvent particle mesh Ewald. J. Chem. Theory Comput. 9, 3878–3888 (2013). [PubMed: 26592383]
48. Case DA et al. AMBER 2018 (Univ. of California, San Francisco 2018).
49. Hopkins CW, Le Grand S, Walker RC & Roitberg AE Long-time-step molecular dynamics through hydrogen mass repartitioning. J. Chem. Theory Comput. 11, 1864–1874 (2015). [PubMed: 26574392]
50. Ryckaert J-P, Ciccotti G & Berendsen HJC Numerical integration of the Cartesian equations of motion of a system with constraints: Molecular dynamics of n-alkanes. J. Comput. Phys. 23, 327–341 (1977).
51. Humphrey W, Dalke A & Schulten K VMD: visual molecular dynamics. J. Mol. Graph. 14, 33–38, 27–28 (1996). [PubMed: 8744570]
52. Roe DR & Cheatham TE III. PTRAJ and CPPTRAJ: software for processing and analysis of molecular dynamics trajectory data. J. Chem. Theory Comput. 9, 3084–3095 (2013). [PubMed: 26583988]

53. Klein U, Gimpl G & Fahrenholz F Alteration of the myometrial plasma membrane cholesterol content with beta-cyclodextrin modulates the binding affinity of the oxytocin receptor. Biochemistry 34, 13784–13793 (1995). [PubMed: 7577971]

54. Yauch RL et al. Smoothened mutation confers resistance to a Hedgehog pathway inhibitor in medulloblastoma. Science 326, 572–574 (2009). [PubMed: 19726788]

55. Buonamici S et al. Interfering with resistance to Smoothened antagonists by inhibition of the PI3K pathway in medulloblastoma. Sci. Trans. Med. 2, 51ra70 (2010).

56. Dijkgraaf GJ et al. Small molecule inhibition of GDC-0449 refractory Smoothened mutants and downstream mechanisms of drug resistance. Cancer Res. 71, 435–444 (2011). [PubMed: 21123452]

57. Atwood S-X et al. Smoothened variants explain the majority of drug resistance in basal cell carcinoma. Cancer Cell 27, 342–353 (2015). [PubMed: 25759020]

58. Sharpe HJ et al. Genomic analysis of Smoothened inhibitor resistance in basal cell carcinoma. Cancer Cell 27, 327–341 (2015). [PubMed: 25759019]

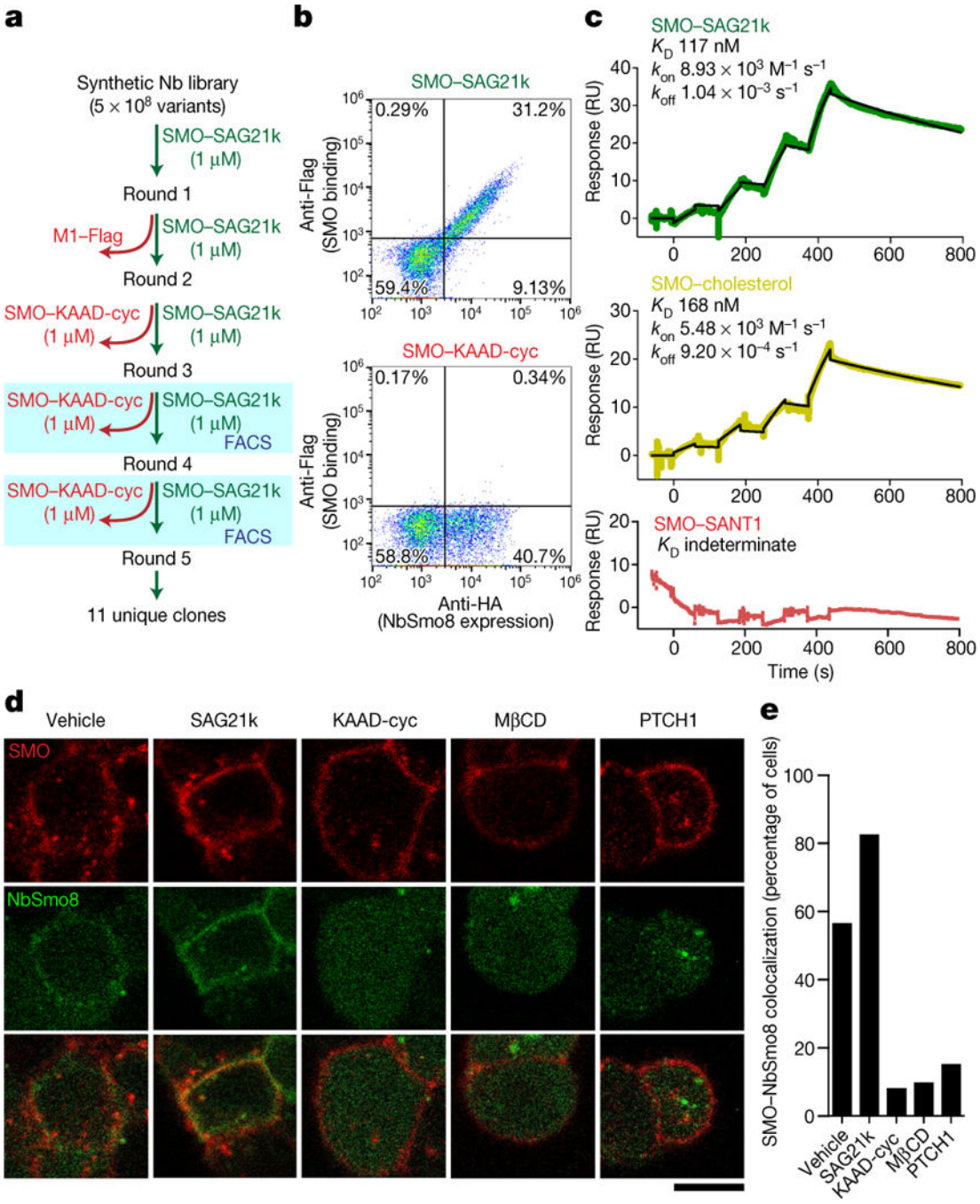

Fig. 1 |. NbSmo8 is a SMO biosensor.

a, Nanobody (Nb)-displaying yeast selective for SAG21k-bound SMO were enriched over multiple rounds. FACS, fluorescence activated cell sorting; KAAD-cyc, KAAD-cyclopamine. **b**, NbSmo8 shows a strong preference for SAG21k-bound SMO. **c**, Surface plasmon resonance of SMO binding to immobilized NbSmo8. No NbSmo8 binding was observed for SANT-1-occupied SMO. RU, resonance units. **d**, NbSmo8-GFP plasma membrane localization in HEK293 cells is dependent on SMO activation. Cells expressing Flag-SMO and NbSmo8-GFP were treated with indicated conditions. Separately, an isogenic

stable cell line that co-expressed PTCH1 with Flag-SMO and NbSmo8-GFP was imaged (PTCH1). Scale bar, 10 μm. **e**, Percentage of cells displaying NbSmo8-GFP at the membrane in **d** (*n* = 29–56 cells per condition). MβCD, methyl-β-cyclodextrin.

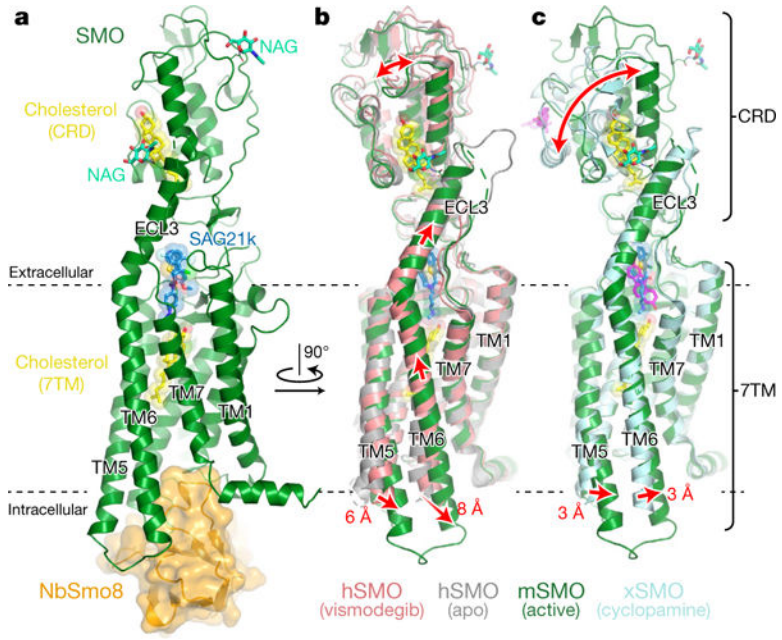

Fig. 2 |. Structure of activated SMO.

a, Overall structure of SMO-SAG21k-NbSmo8 complex bound to two cholesterol molecules. NAG, **N**-acetyl glucosamine. **b**, Comparison of active mSMO to apo and vismodegib-bound hSMO. Large conformational changes in the intracellular domain are coupled with smaller changes within the CRD. Active mSMO shows an upward displacement of TM6 and ECL3 compared with inactive hSMO. **c**, Active mSMO compared to cyclopamine-bound xSMO. Subtle lateral movements in TM5 and TM6 are highlighted.

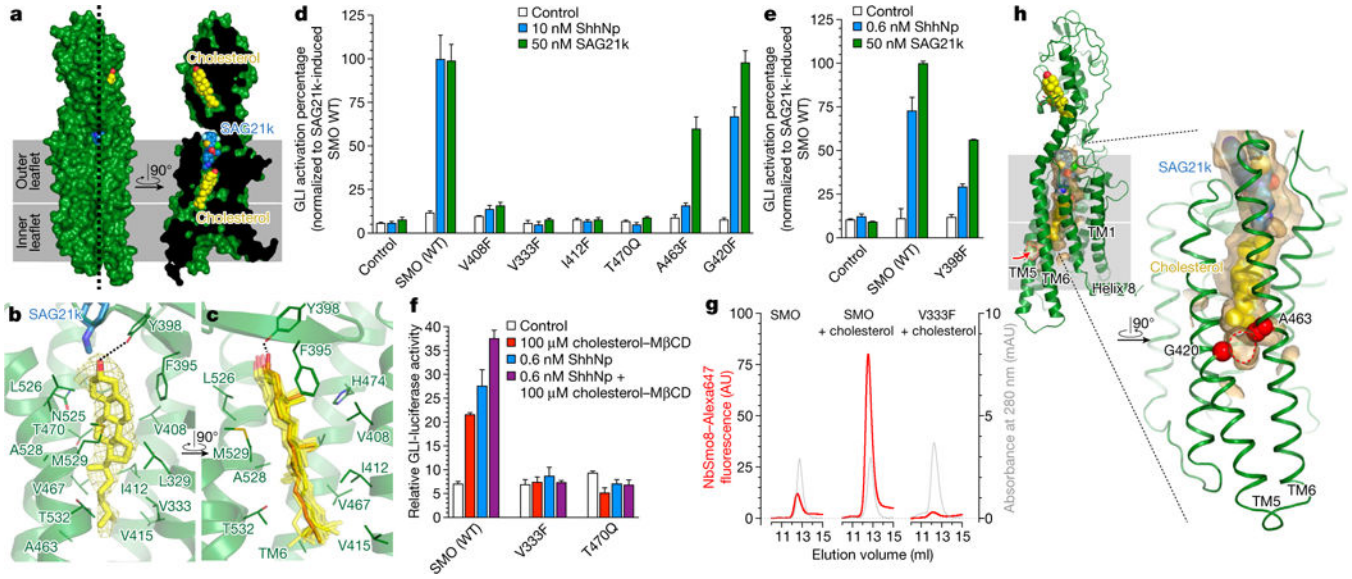

Fig. 3 |. The 7TM sterol site is critical for SMO activation.

a, Surface cut-view, highlighting SMO ligand-binding sites. **b**, $F_o - F_c$ omit density for 7TM cholesterol at 1.5σ (yellow mesh). **c**, Molecular dynamics simulations reveal a stable pose for 7TM cholesterol. Simulation frames sampled every 50 ns are shown as transparent sticks. **d**– **f**, GLI-luciferase signalling assay of SMO mutations at the deep 7TM site or tunnel entrance (**d**), with ablation of the hydrogen bond to Y398 (**e**) or with direct cholesterol–methyl-β-cyclodextrin activation (**f**). WT, wild type. **g**, Fluorescent NbSmo8 co-elutes with SMO in cholesterol-laden micelles. Under identical conditions, the V333F mutant does not bind NbSmo8. AU, arbitrary units; mAU, milli-absorbance units. **h**, A hydrophobic tunnel between TM5 and TM6 connects the inner membrane leaflet to the 7TM pocket. In **d**–**f**, mean ± s.e.m. of n = 3 biological replicates is shown.

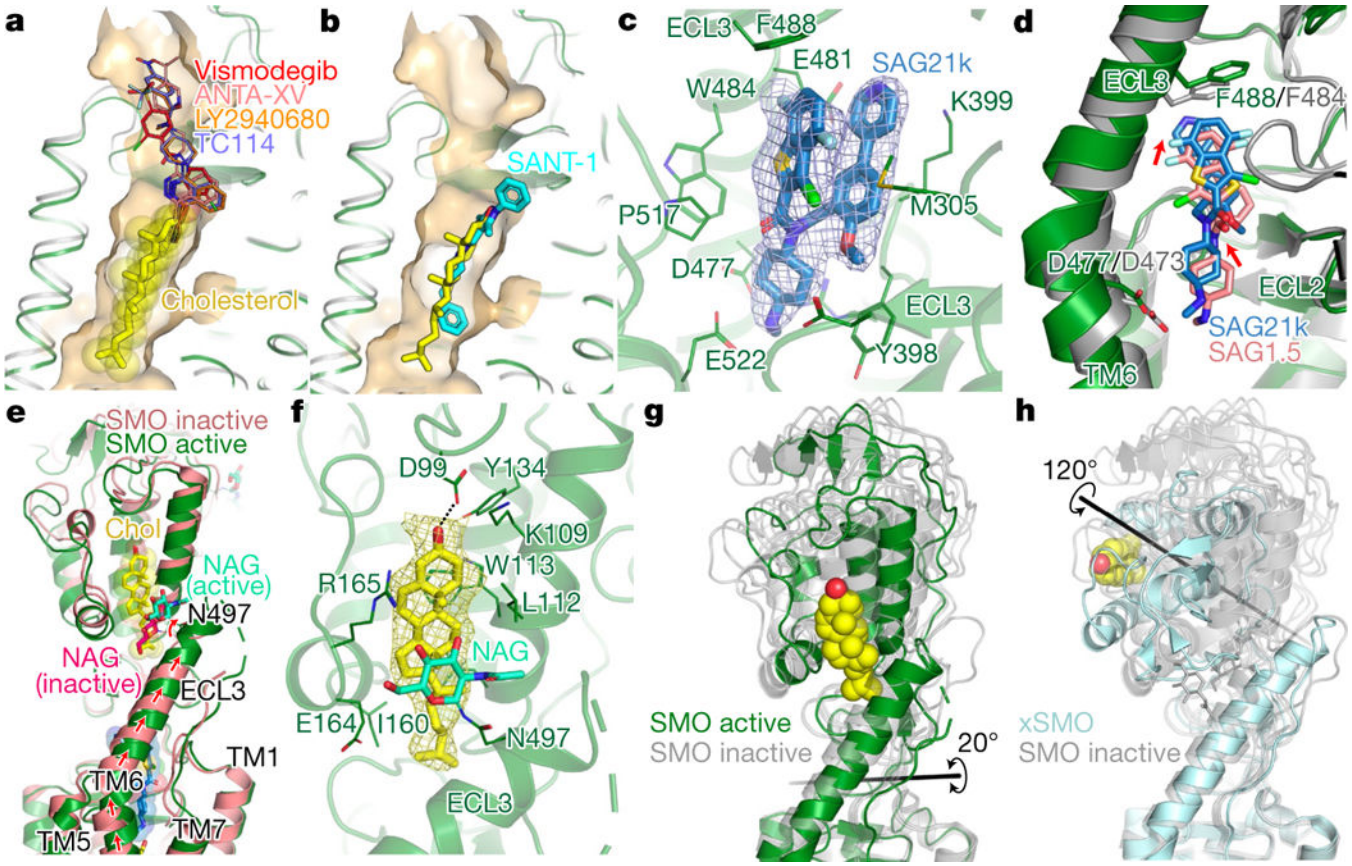

Fig. 4 |. SMO pharmacology at the 7TM and CRD sites.

a, Binding pocket of active SMO with antagonist-bound structures of hSMO overlaid. An antagonist functional group would clash with the 7TM cholesterol. **b**, SANT-1 more closely overlaps with 7TM cholesterol, as compared to the other antagonists. c, F_o — F_c omit density for SAG21k at 2.5σ (blue mesh). **d**, Comparison of SAG21k in active SMO to SAG1.5 bound to inactive SMO (grey). **e**, Comparison of CRD cholesterol (chol) site in inactive and active SMO. **f**, CRD cholesterol $F_o - F_c$ omit density at 1.5σ (yellow mesh). **g**, Comparison of CRD orientations in all hSMO structures (grey) with active mSMO (green). CRD motions in all hSMO and mSMO structures share a common axis (black line) that varies by about 20°. **h**, The 120° CRD rotation observed in xSMO occurs along a unique axis.